Aberrant L-Fucose Accumulation and Increased Core Fucosylation Are Metabolic Liabilities in Mesenchymal Glioblastoma

Valentina Pieri[1,2], Alberto L. Gallotti[1], Denise Drago[3], Manuela Cominelli[4], Ilaria Pagano[1], Valentina Conti[1], Silvia Valtorta[5], Angela Coliva[5], Sara Lago[6], Daniela Michelatti[6], Luca Massimino[7], Federica Ungaro[7], Laura Perani[8], Antonello Spinelli[8], Antonella Castellano[2], Andrea Falini[2], Alessio Zippo[6], Pietro L. Poliani[4], Rosa Maria Moresco[5,9,10], Annapaola Andolfo[3], and Rossella Galli[1]

ABSTRACT

Glioblastoma (GBM) is a common and deadly form of brain tumor in adults. Dysregulated metabolism in GBM offers an opportunity to deploy metabolic interventions as precise therapeutic strategies. To identify the molecular drivers and the modalities by which different molecular subgroups of GBM exploit metabolic rewiring to sustain tumor progression, we interrogated the transcriptome, the metabolome, and the glycoproteome of human subgroup-specific GBM sphere-forming cells (GSC). L-fucose abundance and core fucosylation activation were elevated in mesenchymal (MES) compared with proneural GSCs; this pattern was retained in subgroup-specific xenografts and in subgroup-affiliated human patient samples. Genetic and pharmacological inhibition of core fucosylation significantly reduced tumor growth in MES GBM preclinical models. Liquid chromatography-mass spectrometry (LC-MS)–based glycoproteomic screening indicated that most MES-restricted core-fucosylated proteins are involved in therapeutically relevant GBM pathological processes, such as extracellular matrix interaction, cell adhesion, and integrin-mediated signaling. Selective L-fucose accumulation in MES GBMs was observed using preclinical minimally invasive PET, implicating this metabolite as a potential subgroup-restricted biomarker.

Overall, these findings indicate that L-fucose pathway activation in MES GBM is a subgroup-specific dependency that could provide diagnostic markers and actionable therapeutic targets.

Significance: Metabolic characterization of subgroup-specific glioblastoma (GBM) sphere-forming cells identifies the L-fucose pathway as a vulnerability restricted to mesenchymal GBM, disclosing a potential precision medicine strategy for targeting cancer metabolism.
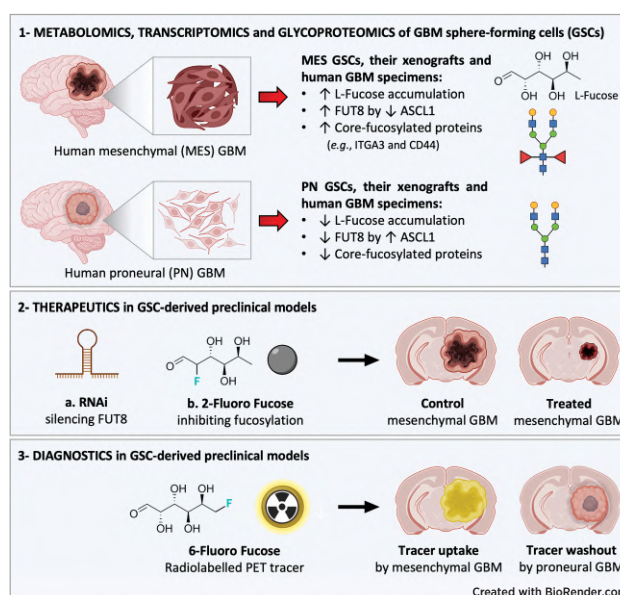
Mesenchymal GSCs are characterized by L-Fucose accumulation and enhanced core fucosylation, which may act as MES GBM-specific diagnostic imaging markers and actionable therapeutic vulnerabilities.

Introduction

Convergent and divergent metabolic phenotypes in cancer are highly relevant both from a mechanistic and therapeutic standpoint. Convergent features are common among distinct cancers and include core pathways controlling energy production, macromolecule synthesis, and cellular homeostasis (1). Conversely, divergent features involve heterogeneously activated pathways, leading to subtype-selective phenotypes, such as 2-hydroxyglutarate (2HG) accumulation. Although convergent and divergent metabolic

[1]Division of Neuroscience, Neural Stem Cell Biology Unit, IRCCS San Raffaele Hospital, Milan, Italy. [2]Neuroradiology Unit and CERMAC, Vita-Salute San Raffaele University and IRCCS San Raffaele Hospital, Milan, Italy. [3]ProMeFa, Center for Omics Sciences, IRCCS San Raffaele Hospital, Milan, Italy. [4]Molecular and Translational Medicine Department, Pathology Unit, University of Brescia, Brescia, Italy. [5]Nuclear Medicine and PET Cyclotron Center, IRCCS San Raffaele Hospital, Milan, Italy. [6]Department of Cellular, Computational and Integrative Biology (CIBIO), Laboratory of Chromatin Biology & Epigenetics, University of Trento, Trento, Italy. [7]Gastroenterology and Endoscopy Department, Experimental Gastroenterology Unit, IRCCS San Raffaele Hospital, Milan, Italy. [8]Experimental Imaging Center, IRCCS San Raffaele Hospital, Milan, Italy. [9]Institute of Bioimaging and Molecular Physiology (IBFM), CNR, Segrate, Italy. [10]Department of Medicine and Surgery and Tecnomed Foundation, University of Milano—Bicocca, Monza, Italy.

Corresponding Author: Rossella Galli, IRCCS San Raffaele Hospital, Via Olgettina 58, 20132 Milan, Italy. Phone: 3902-2643-4626; E-mail: galli.rossella@hsr.it

phenotypes can both generate metabolic vulnerabilities, only the latter may provide liabilities to be exploited in precision medicine approaches.

Tumors originating in the same tissue but characterized by distinct molecular and histological features may be endowed with different metabolic properties (1–3). This concept may apply also to glioblastoma (GBM), the deadliest brain tumor of adults. On the basis of bulk transcriptomics, IDH1–wild-type GBMs (4) fall into three distinct subgroups, that is, proneural (PN), classical (CL), and mesenchymal (MES; refs. 5, 6). Recently, single-cell/single-nuclei RNA sequencing (scRNA-seq/snRNA-seq)–based studies indicated that GBMs present with a significant intratumor heterogeneity (7), being better defined as a mixture of cells expressing distinct transcriptional signatures (8, 9). Thus, multiple molecular and cellular states are in place in each different GBM.

Although MES GBMs have been linked to worse prognosis and therapy resistance (10), to date GBM transcriptional subgroups have limited clinical relevance. Nonetheless, the inclusion of additional layers of molecular information, for example, the identification of subgroup-restricted metabolic features, may increase the chances for GBM subgrouping to inform future treatment decisions.

In the last years, several studies investigated the contribution of metabolic dysfunction in GBM and, specifically, in GBM stem cells. As an example, de novo purine, pyrimidine, and mevalonate pathways are upregulated in GBM stem cells and correlate with poor patient survival (11–13). Likewise, alterations in lipid metabolism drive stem-cell enrichment and GBM progression (14, 15). Thus, GBM stem cells are endowed with a remarkable metabolic flexibility that enables them to adjust to different types of microenvironment-dependent and therapy-induced metabolic stress and provides putative metabolic vulnerabilities for GBM treatment.

Although a link between the upregulation of specific metabolic pathways in GBMs and in GBM stem cells and the presence of specific genetic mutations and/or transcriptional phenotypes has been lately documented (16–18), there is still much to be understood concerning the relationship between metabolic dysregulation and transcriptional subtypes in GBM.

Within this frame of reference, to identify metabolic candidates that might enable precision targeting of subgroup-restricted metabolism in GBM, we exploited PN and MES patient-derived GBM sphere-forming cell (GSC) lines and interrogated their metabolic profiles. By integrating bulk RNA-seq and untargeted metabolomics, we pinpointed L-Fucose and core fucosylation as relevant metabolic vulnerabilities in MES GBMs.

L-Fucose is a levorotatory sugar that is incorporated into N-, O- or lipid-linked oligosaccharide chains by means of terminal and core fucosylation (19). These processes are orchestrated through the synthesis of the intermediate GDP–L-Fucose that is transferred from the cytoplasm to the Golgi by the transporter SLC35C1 and, once there, is conjugated on glycan chains by fucosyltransferases (FUT). Most GDP–L-Fucose synthesis takes place de novo from GDP-mannose through GDP-mannose–phosphorylase A (GMPPA), GDP-mannose 4,6-dehydratase (GMDS) and tissue specific transplantation antigen p35B (TSTA3) activation. The rest of the GDP–L-Fucose synthesis relies on the salvage pathway, in which GDP–L-Fucose is generated from the free L-Fucose derived from dietary intake by fucose kinase (FUK) and fucose-1-phosphate guanylyltransferase (FPGT) or from lysosomal breakdown of fucosylated proteins by alpha–L-fucosidase (FUCA1).

The $\alpha1$–6 fucosyltransferase FUT8 catalyzes the core fucosylation of the innermost GlcNAc residue of N-glycans at C6 position. Increased FUT8 expression and core fucosylation are detected in hepatocellular carcinoma (HCC; ref. 20), melanoma (21), prostate (22), and breast cancer (23), in which they promote proliferation, invasion, metastatic potential, and resistance to therapy. For instance, core fucosylation of cadherins and integrins decreases cell adhesion and promotes tumor cell migration, and invasion (21, 24), implying core fucosylation as a modality to further promote the malignant function and activity of specific glycoproteins.

Although high FUT8 levels have been described previously in glioma cell lines (GCL) in vitro (25), a comprehensive characterization of L-Fucose pathway activation in GSCs and in human GBMs has not yet been reported. Here, we performed a functional analysis of the L-Fucose pathway and FUT8-dependent fucosylation by subjecting subgroup-specific GSC lines in vitro and their related in vivo preclinical models to high-throughput transcriptomics, metabolomics, and glycoproteomics, whose results concurred to identify dysregulated L-Fucose accumulation and enhanced core fucosylation as selective diagnostic markers and druggable targets in MES GBM.

Materials and Methods

Ethics statement

All animal experiments were approved by and performed in accordance with the guidelines of the International Animal Care and Use Committee and conformed to the Italian Ministry of Health guidelines for animal welfare.

The retrospective study on human GBM samples ($n = 15$ from University of Brescia) was conducted in compliance with the Declaration of Helsinki and with policies approved by the Ethics Boards of Spedali Civili of Brescia, University of Brescia (Brescia, Italy). Specifically, for the retrospective and exclusively observational study on archival material obtained for diagnostic purposes, written informed consent from patients was not needed (Italian Data Protection Authority resolution: # 52, 24/7/2008 and DL 193/2003).

Cell culturing

Human GSCs were cultured in suspension as neurospheres under mild hypoxic conditions (5% O_2) in standard medium containing human recombinant EGF (#AF-100–15, Peprotech; 20 ng/mL) and FGF2 (#100–18B, Peprotech; 10 ng/mL), as described in ref. (26). Human U87 (RRID:CVCL_0022) and U251 (RRID:CVCL_0021) GCLs were grown as adherent monolayer in DMEM containing 10% FCS. For sugar supplementation studies, L-Fucose (#F2252, Sigma-Aldrich) was added to the growth medium for 48 hours at a final concentration of 100 µmol/L.

Untargeted metabolomics on GCLs and GSCs

PN GSCs ($n = 4$) and MES GCLs/GSCs ($n = 4$) were subjected to untargeted metabolomics for polar (aminoacids, nucleotides and sugars) and apolar (fatty acids and membrane lipids) molecules. An extraction solvent of 2:2:1 MeOH/EtOH/H_2O was added to the cell pellets (2×10^6 cells each) and used to generate a single fraction, which contained a mixture of polar and nonpolar lipid metabolites. One mL of MeOH/EtOH/H_2O (2:2:1) was used and two to three freeze–thaw cycles were necessary for cell lysis (750 µL of extraction buffer were used in each freeze–thaw cycle). Proteins and other macromolecules were precipitated after mixing rigorously by vortex for 2 minutes and centrifuged at 14,000 × g at 4°C for 5 minutes. The supernatant was collected, dried under nitrogen, and resuspended in 300 µL of 60% ACN/H_2O. Relative levels of each metabolite were profiled by LC/MS-MS using 3 technical replicates for each sample. Samples were analyzed

using the UPLC 1290 (Agilent Technologies) coupled to the Triple Time of Flight (TOF) 5600+ mass spectrometer (SCIEX; ProMeFa, Proteomics and Metabolomics Facility, Ospedale San Raffaele, Milan, Italy). Chromatographic separations occurred on C18 column (ACQUITY UPLC HSS T3 Column, Waters, 1.8 μm, 2.1 mm × 100 mm) by directly injecting 10 μL of samples. Metabolites were separated using a flow rate set at 0.6 mL/min and a gradient of solvents A (water, 0.1% formic acid) and B (methanol, 0.1% formic acid). The gradient, in both the positive and negative mode, started from 2% B, increased up to 95% B in 14 minutes, remained constant at 95% B for 5 minutes, decreased to 2% B in 0.5 minutes, and remained at 2% for 2 minutes. The column was set at 50°C, whereas the samples were kept at 4°C. UPLC was also performed on aqueous extracts using an ACQUITY UPLC BEH HILIC column (Waters, 1.7 μm, 2.1 mm x 100 mm) by directly injecting 5 μL of samples. The flow rate was 0.6 mL/min with mobile phase A (acetonitrile, 0.1% formic acid) and mobile phase B (water, 0.1% formic acid). The gradient in both positive and negative mode started from 2% B, increased up to 60% B in 10 minutes, remained constant at 60% B for 2 minutes, decreased to 2% B in 0.5 minutes, and remained at 2% for 2.5 minutes. The column was set at 40°C, whereas the samples were kept at 4°C. Full-scan spectra were acquired in the mass range from m/z 50 to 500. Automated calibration was performed using an external calibrant delivery system that infuses APCI-positive or -negative calibration solution every 5 samples injection. A TOF MS survey scan experiment with an IDA set to monitor 6 most intense candidate ions was performed. The six most intense ions were selected and fragmented. The source parameters were: Gas 1: 33 psi, Gas 2: 58 psi, Curtain gas: 25 psi, Temperature: 500°C and ISVF (IonSpray Voltage Floating): 5500 V in positive mode (4500 V in negative mode), DP: 80 V, CE: 44 V. Data were processed using MasterView Software (SCIEX) for the metabolite identification with the Accurate Mass Metabolite Spectral Library (SCIEX). Marker-View Software was also used for simultaneous feature finding, alignment, and statistical analysis to highlight metabolites of interest. Significant metabolites for each experimental comparison ($P < 0.05$ from t test performed in MarkerView) were used to perform principal component analysis (PCA). TM4 Microarray Software Suite—TIGR MultiExperiment Viewer (v 4.9.0; RRID:SCR_001915) was used for hierarchical clustering heatmap of peak intensities of the significant differentially regulated metabolites among experimental conditions, performed using Pearson correlation metric ($P \leq 0.05$). Metabolite set enrichment analysis was also carried out by using MetaboAnalyst v5.0 software (RRID:SCR_015539). Enriched pathways were ranked according with their FDR values calculated by the MetPa method implemented in MetaboAnalyst (RRID:SCR_015539).

RNA-seq

RNA from PN and MES GSCs was extracted by using the RNeasy mini kit (#74104, Qiagen) according to the manufacturer's protocol. The cDNA was synthesized starting from total RNA using SMART technology. After barcoding, the RNA libraries were pooled, denatured, and diluted to 2.4 pmol/L final concentration. RNA-seq was performed by using NextSeq 550 (Illumina) set for 76 cycles in single end (SE), yielding an average of 15×10^6 clusters for each sample. Sequences were aligned using STAR v2.5.3a (RRID:SCR_004463) on the reference genome GRCh38; association between reads and genes has been performed by feature counts, using gencode (version 28) basic annotation as reference. Analysis of count data was performed using the DESeq2 (differential gene expression analysis based on the negative binomial distribution) pipeline v1.6.3 (RRID:SCR_000154). The independent filtering of genes with low counts was set to a mean of 9 raw

counts between all samples. The cutoff value imposed for differential gene expression was the one suggested by the SEquencing Quality Control consortium, which defines a gene as differentially expressed when it has an associated raw P value of lower than 0.01 and, at the same time, the absolute value of its $\log_2$FC is greater than 1 ($\log_2$FC > 1 or $\log_2$FC < −1).

Bioinformatics

For expression analysis on GSC datasets, normalized count matrices were retrieved from the NCBI GEO repository by GEOquery (RRID: SCR_000146), annotated with biomaRt (RRID:SCR_019214), and visualized with ggplot2 (RRID:SCR_014601). Differential gene expression was performed with GEO2R (https://www.ncbi.nlm.nih.gov/geo/geo2r/; RRID:SCR_016569).

For single-cell expression analysis, the expression of the genes encoding for the enzymes in the L-fucose metabolic pathway was analyzed in the single-cell expression dataset SCP503 (27), by the Single-Cell Portal of the Broad Institute (https://singlecell.broadinstitute.org/single_cell).

For the Pearson correlation analysis, raw data from distinct patients' GBM datasets, publicly available at the GlioVis data portal for visualization and analysis of brain tumor expression datasets (28), were downloaded and prepped for further analyses. Pairwise correlation between the eight genes in the L-Fucose pathway was measured with a Pearson's coefficient. Analyses were executed with R Project for Statistical Computing (RRID:SCR_001905), RStudio (RRID: SCR_000432) and appropriate R packages, such as dplyr (RRID: SCR_016708), stringr v1.4.0, ggplot2 and GGally v2.1.2.

Quantitative PCR analysis

Total RNA from PN GSCs and MES GCLs/GSCs was extracted using the RNeasy Mini kit (#74104, Qiagen). One μg of total RNA was reverse-transcribed by using High-Capacity cDNA Reverse Transcription Kit (#4368814, Applied Biosystems, Thermo Fisher Scientific). qRT-PCR was performed by using GoTaq qPCR Master Mix (#A6001, Promega), following the manufacturer's instructions. KiCqStart SYBR Green human-specific primers were purchased from Sigma-Aldrich. β-Actin was used as housekeeping gene. The data shown represent duplicate qPCR measurements of 4 biological replicates for each subgroup of GCLs/GSCs.

Western blotting

Each frozen cell pellet was homogenized in 10× volume of RIPA lysis buffer (10 mmol/L Tris-Cl pH 7.2, 150 mmol/L NaCl, 1 mmol/L EDTA pH 8) with 1% Triton X-10/0.1% deoxycholate, 0.1% SDS, and protease and phosphatase inhibitor mixture (Roche). Samples were then diluted in Laemmli's SDS sample buffer. Proteins were separated by electrophoresis on 10% polyacrylamide gels according to the TGX Stain-Free FastCast Acrylamide kit (#1610182, Bio-Rad) and transferred onto Trans-Blot nitrocellulose membranes (#1704159, Bio-Rad) according to the Trans-Blot Turbo Transfer System kit protocol (Bio-Rad). Ponceau staining (#P7170–1L, Sigma-Aldrich) was performed to assess correct protein transfer and equal loading of total protein The membranes were blocked in 5% nonfat dry milk in TBST (pH 7.4, with 0.1% Tween-20) for 1 hour at room temperature. The primary antibodies used, that is, sheep anti-FUT8 (R&D Systems Cat# AF5768, RRID:AB_2105499, 1:400); rabbit anti-CD44 (Cell Signaling Technology Cat# 37259, RRID:AB_2750879, 1:1,000); mouse anti-ITGA3, Abcam, Cat# ab242196, RRID:AB_2920907, 1:1,000, Abcam; anti-MASH1/ASCL1 (BD Biosciences Cat# 556604, RRID: AB_396479, 1:200); rabbit anti-NDRG1 (Cell Signaling Technology

Cat# 9408, RRID:AB_11140640, 1:1,000); rabbit anti-calnexin (GeneTex Cat# GTX13504, RRID:AB_368878, 1:3,000), and mouse anti–β-tubulin (Covance Cat# MMS-410P-250, RRID:AB_10063407, 1:500) were diluted in 3% BSA (Sigma-Aldrich) in TBST. The primary antibody was removed, and the blots were washed in TBST and then incubated for 1 hour at room temperature in horseradish peroxidase (HRP)–conjugated anti-mouse (Bio-Rad Cat# 170–6516, RRID:AB_11125547, 1:2,000), anti-rabbit (Bio-Rad Cat# 170–6515, RRID:AB_11125142, 1:2,000), and anti-sheep (R&D Systems Cat# HAF016, RRID:AB_562591, 1:1,000) secondary antibodies. Reactive proteins were visualized using a Clarity Western ECL substrate kit (#1705061, Bio-Rad), and exposure was performed using UVItec (Cambridge MINI HD). Images were acquired by NineAlliance software. The data shown represent duplicate/triplicate measurements of 4 biological replicates for each subgroup of GCLs/GSCs.

Immunostaining on paraffin-embedded sections

For CD44 and ITGA3 staining, we used the same rabbit anti-CD44 and mouse anti-ITGA3 antibodies mentioned above. From formalin-fixed paraffin-embedded (FFPE) mouse and human tumor samples, 3-μm sections were cutoff, dewaxed, rehydrated, and heat-induced antigen retrieval was performed using a thermostatic bath in 1 mmol/L Citrate (pH 6.0) buffer. Sections were then washed in TBST (pH 7.6, Dako Wash Buffer, 1X; #S3006, Agilent) and endogenous peroxidase activity was blocked by 3% H_2O_2 for 30 minutes. Nonspecific binding was reduced by blocking with Protein Block (Rabbit specific HRP/DAB (diaminobenzidine) Detection IHC Detection Kit Micro-polymer, #ab236469, Abcam) and Mouse-on-mouse blocking reagent (Mouse-on-Mouse Polymer IHC Kit, #ab269452, Abcam) for 30 minutes at room temperature, respectively. Sections were washed in TBST and then incubated overnight with the primary antibodies, diluted in Dako Antibody Diluent with Background Reducing Components (#S3022, Agilent). Slides were then washed in TBST and incubated for 30 minutes with Goat Anti-Rabbit HRP-Conjugate or 15 minutes with HRP Polymer Detector provided within the above-mentioned kits.

For FUT8 staining, we used the same sheep anti-FUT8 used in Western blotting (WB). From FFPE human adult healthy brain as well as mouse and human tumor samples, 2-μm sections were cut, dewaxed, rehydrated, and endogenous peroxidase activity blocked by 0.3% H_2O_2/methanol for 20 minutes. Heat-induced antigen retrieval was performed using a thermostatic bath in 1.0 mmol/L EDTA (pH 8.0) buffer. Sections were then washed in TBS (pH 7.4) and incubated for 1 hour or overnight in TBS/1% BSA with the primary antibody. Slides were then incubated for 30 minutes with the biotinylated anti-sheep secondary antibody (Vector Laboratories Cat# BA-6000, RRID:AB_2336217), and then with HRP-conjugated streptavidin (#P0397, Dako) for 45 minutes. Immunostaining was revealed by DAB (#ab64238, Abcam) as chromogen and hematoxylin as counterstaining.

All histological and IHC staining results were reviewed independently by two pathologists that were blinded to the identity and clinicopathological information of the samples. Human samples were classified on the basis of an integrated molecular and IHC-based algorithm that performs a high-accuracy prediction of GBM transcriptional subtypes, that is, PN, CL, and MES (29).

Lectin histochemistry

From FFPE mouse and human tumor samples, 3-μm sections were cut, dewaxed, rehydrated, and heat-induced antigen retrieval was performed using a thermostatic bath in 1.0 mmol/L EDTA (pH 8.0) buffer. Endogenous peroxidase activity was blocked by 0.3% H_2O_2 for

30 minutes and nonspecific binding was reduced by blocking with 5% nonfat dry milk in TBST (pH 7.6, Dako Wash Buffer, 1X; Agilent) for 1 hour at room temperature. Sections were washed in TBST and then incubated with biotinylated Aleuria Aurantia Lectin (AAL; Vector Laboratories Cat# B-1395, RRID:AB_2336084) diluted at 1:100 in TBST/5% nonfat dry milk overnight at 4°C. Detection of biotinylated lectins was performed using HRP-conjugated streptavidin (BD Biosciences Cat# 554066, RRID:AB_2868972) diluted at 1:600 in Dako Antibody Diluent with Background Reducing Components (Agilent) for 40 minutes at room temperature followed by DAB as chromogen and hematoxylin as counterstaining.

Lectin blotting

Sample homogenization and dilution, protein separation by electrophoresis, gel transfer on nitrocellulose membranes, and Ponceau staining were performed as described previously for standard WB. The whole membranes were blocked in 5% nonfat dry milk in TBST (pH 7.4, with 0.1% Tween-20) for 1 hour at room temperature. AAL was diluted 1:2,000 in 3% BSA, and the membranes were incubated overnight at 4°C with gentle agitation. AAL was removed, and the blots were washed in TBST and then incubated for 1 hour at room temperature with HRP-conjugated streptavidin (#SA10001, Invitrogen). Reactive proteins were visualized using the Clarity Western ECL substrate kit (Bio-Rad), and exposure was performed using UVItec (Cambridge MINI HD). Images were acquired by NineAlliance software.

Immunofluorescence for lectins

Immunofluorescence (IF) was performed on undifferentiated PN GSCs and MES GCLs/GSCs, plated at 3.5×10^5 cells/cm^2 on glass coverslips coated with growth factor–reduced Matrigel (#354230, Becton and Dickinson) for 24 hours in proliferation medium and then fixed with 4% PFA for 20 minutes at room temperature.

For intracellular epitopes detection, cells were permeabilized for 10 minutes with 0.1% Triton X-100 in PBS. Cells were then incubated with biotinylated AAL (Vector Laboratories) diluted at 1:50 in PBS containing 10% normal goat serum over night at 4°C followed by TRITC-conjugated streptavidin (#43–4314, Thermo Fisher Scientific) for 1 hour at room temperature. Nuclei were counterstained with 4′,6-diamidino-2-phenylindole dihydrochloride (#32670, Sigma-Aldrich).

Image data acquisition and analysis

For standard IHC-staining acquisition and quantification, images were acquired at ×40 magnifications by a Nikon camera mounted on Nikon microscope using the NIS-Elements software. Image analysis was performed by using the open-source image processing package ImageJ-Fiji (RRID:SCR_002285)

Gene silencing

LV particles coding for shRNA clones targeted against human *FUT8* were purchased from Sigma-Aldrich (Mission RNAi). Transduction of GSCs was performed with two different types of controls, namely the Empty Vector Control (SHC001V; TRC1.5-pLKO.1-puro), as a negative control that will not activate the RNAi pathway because it does not contain an shRNA insert, and the Non-Targeting shRNA Control (SHC002V), as a negative control that will activate RISC and the RNAi pathway but does not target any human or mouse genes, and 5 different clones for human *FUT8* and *ASCL1* at MOI 5 overnight. Cells were subcultured for at least 4 passages before starting selection by adding puromycin (1 μg/mL) to the culture medium. Silencing efficiency was assessed by WB and the two clones showing the highest knockdown efficiency were selected for subsequent analysis (*FUT8*:

clones #TRCN0000035952 and #TRCN0000229961 for U87 GCLs and L1312 GSCs; clones #TRCN0000229959 and #TRCN0000229961 for L0315 GSCs; *ASCL1*: clones # TRCN0000013550 and # TRCN0000013551 for L0627 GSCs).

Limiting dilution neurosphere formation assay

For *in vitro* limiting dilution assay, 7-aminoactinomycin D–negative MES GSCs were sorted by FACS and decreasing numbers of cells (100, 50, 20, 10, 5, and 1) were plated in 96-well plates containing complete medium. Fourteen days after plating, the cell content in each well was recorded by the Incucyte Live-Cell Analysis system (Sartorius). The number of GBM spheres in each well was exploited for standard-limiting dilution clonogenic assays, whereas the number of wells containing or not neurospheres was used for the extreme-limiting dilution analysis (ELDA). Sphere-forming cell frequency was calculated using the ELDA software (https://bioinf.wehi.edu.au/software/elda/; RRID:SCR_018933).

Long-term population analysis

To monitor the effect of gene silencing on GSC self-renewal, a long-term population analysis was performed by plating cells at 8×10^3 cells/cm^2 density. The resulting neurospheres were collected every 3 to 5 days and dissociated into single cells. The total number of viable cells was assessed by Trypan Blue (#T8154, Sigma-Aldrich) exclusion. At each subculturing passage, the relative amplification rate was calculated by dividing the amount of the viable counted cells by the number of cells originally seeded. The amplification rate was then multiplied for the total number of cells as detected at the previous subculturing passage, and the final number of cells plotted in correspondence of the last subculturing passage. By this way, a growth curve was generated for each experimental condition (30).

Evaluation of tumorigenicity

For intracranial transplantation, 3×10^5 MES GCLs and 4×10^5 human PN and MES GSCs were transferred in 3 and 4 μL of DMEM containing DNase, respectively, and delivered into the right striatum of deeply anesthetized, immunocompromised NOD.Cg-Prkdc^{scid} Il2rg^{tm1Wjl}/SzJ (RRID:IMSR_JAX:005557; NSG) female mice at 6–8 weeks of age (Charles River Laboratories) by stereotactic injection through a 5-μL Hamilton micro-syringe at a flow rate of 0.5 μL/min. The following coordinates were used: AV = 0; ML = +2.5 mm; DV = −3.5 mm from bregma. Animals were sacrificed at different time points after transplantation.

MRI

All the MRI studies were performed on a small animal-dedicated 7T scanner (30/70 BioSpec; Bruker, Ettlingen, Germany). During image acquisition, the animals were kept at 37°C under gaseous anesthesia (2%–3% isoflurane and 1 L/min oxygen). The animal protocol used to monitor tumor development in NSG mice included high-resolution T2-weighted sequences (TR/TE = 3,000/12 ms, matrix = 170×170, voxel size = 0.11 mm^2, section thickness = 0.75 mm). After converting Bruker images into the nifti format with MATLAB (RRID: SCR_001622), tumor masses were manually segmented using ITK-SNAP (RRID:SCR_002010). Tumor volumes were then calculated by means of the "*fslstats*" tool of FSL (RRID:SCR_002823).

In vivo bioluminescence imaging

Bioluminescence optical imaging (BLI) was performed using a dedicated small animal optical imaging system (IVIS Spectrum, PerkinElmer). The IVIS Spectrum is based on a cooled (−90°C) CCD camera with an active array of 2048 × 2048 pixels with a dimension of 13 μm and a quantum efficiency in the visible range above 85%. Images corrected for dark measurements were acquired using the following parameters: Exposure time, auto; aperture f, 1; binning B, 8; and field of view FoV, 22 cm (field D). Each mouse received an intraperitoneal injection of 150 mg luciferin/kg body weight, 10 minutes before BLI. During image acquisition, the animals were kept at 37°C under gaseous anesthesia (2%–3% isoflurane and 1 L/min oxygen). Dynamic BLI was performed by acquiring a set of images every 2 minutes from 10 to 20 minutes after luciferin injection to detect the highest BLI signal. BLI analysis was performed by placing region of interests (ROI) and by measuring the total flux (photons/seconds) within the ROI using Living Image 4.5 software (RRID:SCR_014247). To monitor tumor development in all the experimental groups, BLI was performed every two to three days up to 16 days for U87-derived xenografts, and once a week up to 19 weeks for 1312-derived xenografts.

Treatment of human GCLs/GSCs with 2-fluorofucose *in vitro* and MTT viability assay

GSCs were seeded in Matrigel-coated wells of 96-well plates at a density of 1.5×10^4 cells/well in standard stem cell medium supplemented or not with 2-deoxy-2-fluoro-L-Fucose (2-fluorofucose, 2FF; #MD06089, Carbosynth Limited) and incubated at 37°C. Dimethyl sulfoxide (DMSO, #D2650, Sigma-Aldrich) was used as vehicle. After 48 and 72 hours, 25 μL of (3-(4,5-dimethylthiazol-2-yl)-2,5-diphenyltetrazolium bromide (MTT) solution (#M5655, tetrazolium salt; 5 mg/mL in PBS; Sigma-Aldrich) was added to each well and the plates were incubated for 1 hour at 37°C, to allow the deposition of formazan crystal salts in the mitochondria of viable cells. The medium was then removed, and cells were lysed with DMSO to allow crystal dissolution. Cell survival was determined as the absorbance at 570-nm wavelength by means of a microplate reader.

Treatment of human GSC/GCL-derived GBM xenografts with 2-fluorofucose *in vivo*

For *in vivo* administration experiments, 2-fluorofucose (2FF) was dissolved in DMSO at a 100 mmol/L concentration, stored at −20°C, and diluted in a DMEM-based vehicle solution immediately before loading into ALZET Osmotic Pumps. Transplanted NSG female mice were randomized on the basis of MRI volumetric analysis. Inclusion criterion was based on an average tumor volume of 2 mm^3. Mice were treated through pumps with the drug or vehicle for 2 weeks (U87 cells) or 8 weeks (L1312 GSCs). See Supplementary Table S2 for a detailed description of doses and delivery rates used.

Chromatin immunoprecipitation assay

Each chromatin immunoprecipitation (ChIP) experiment was performed in at least three independent biological samples and performed as previously described (31). Briefly, 1×10^6 PN GSCs, either naïve or overexpressing *ASCL1*, were cross-linked with 1% formaldehyde for 10 minutes at room temperature and the reaction was quenched by glycine at a final concentration of 0.125 mol/L. Cells were lysed in lysis buffer and chromatin was sonicated. 5% of the sonicated material was saved as DNA input. Fragmented chromatin samples were incubated 4 hours at 4°C with protein G–coated magnetic beads (Invitrogen), previously functionalized with the following antibodies: anti-IgG (Millipore Cat# 401411–1ML, RRID:AB_10681263) and anti-MASH1/ASCL1 (BD Biosciences Cat# 556604, RRID:AB_396479). Immunoprecipitated DNA was purified using AMPure XP beads (Beckman-Coulter) and analyzed by qPCR by using SensiFAST SYBR kit (Bioline). Primers set for target regions were designed on the basis of previously published ChIP-seq data of ASCL1 that were available in GEO (accession number: GSE46014, GSE61197, GSE69398, and

GSE87618). The data shown represent triplicate qPCR measurements of the immunoprecipitated DNA. The data are expressed as the percentage of the DNA inputs after correction for input dilution.

Wound-healing assay

The assay was performed according to the IncuCyte live-cell analysis migration assay protocol. Each well in 96-well ImageLock plates was coated with 100 μL of Matrigel overnight to ensure cell attachment. A total of 2.5×10^4 GSCs were plated in each well in 150 μL of complete medium. When cells reached 100% confluence, a scratch was made by the 96-pin IncuCyte WoundMaker and the plate positioned in the IncuCyte instrument, to monitor their migration by time-lapse for up to 72 hours. The temporal progression of wound closure in each well was determined by using the relative wound density as the metric to measure invasion.

Core-fucosylated glycoproteomics and LCA affinity enrichment

Cell pellets from PN GSCs and MES GCLs/GSC lines ($n = 3$ for each subtype) were subjected to glycoproteomic screening by a protocol modified from (32). Pellets were first denatured in 0.5 mL of 8 mol/L urea in Tris HCl pH 7.6 with the addition of protease inhibitors (Halt Protease Inhibitor Cocktail; 100X; Thermo Fisher Scientific) and of phosphatase inhibitors (PhosStop, Merck), and then sonicated thoroughly for 3 minutes. Protein concentration was measured using a BCA protein assay kit (Thermo Fisher Scientific). One mg of total proteins was then reduced by incubation with 10 mmol/L DTT for 1 hour at 56°C and alkylated by addition of 27 mmol/L iodoacetamide at room temperature for 30 minutes in ammonium bicarbonate buffer (ABC) 0.1 mol/L. The sample was diluted 1:4 with ABC buffer 0.1 mol/L, added with 1:50 w/w (20 μg for 1 mg of proteins) sequence-grade trypsin (Sigma-Aldrich), and incubated at 37°C overnight. Peptides were then purified and desalted with OASIS PRIME HLB C18 cartridges (Waters). The samples were eluted in 1 mL (twice 0.5 mL) of ACN/MeOH 90/10 and dried under nitrogen. The agarose bound LCA (Lens Culinaris Agglutinin) was prepared from biotinylated LCA conjugate (Vector Laboratories) and Streptavidin agarose. Before use, 0.1 mL high-capacity streptavidin agarose (Pierce) was washed twice with 0.5 mL PBS to remove sugars added to stabilize the lectin. The agarose was incubated in 0.5 mL PBS with 1 mg of biotinylated LCA for 1 hour at room temperature. The agarose-bound LCA was washed 3 times with 0.5 mL TBS and incubated with the desalted peptides in 0.5 mL of TBS buffer at 4°C overnight. LCA-conjugated samples were then centrifuged for 1 minute at 2,500 × g and the supernatant was removed and used to follow the unbound proteins. The precipitates were washed four times with 0.5 mL TBS buffer by centrifugation at 2,500 × g. After removing the final wash supernatant, 0.5 mL of elution buffer (mixture of 200 mmol/L α-methyl mannoside and 200 mmol/L α-methyl glucoside in TBS for LCA) was added before vortexing for 30 seconds. The supernatant was collected after centrifugation and the precipitate was eluted an additional time. The eluted solutions were combined and desalted with OASIS PRIME HLB C18 cartridges (Waters). The samples were resuspended in 95% ACN/1% TFA and further enriched by OASIS MAX cartridges (Waters). For MAX enrichment, the cartridges were conditioned three times with solutions of ACN, 100 mmol/L triethylammonium acetate, water and 95% ACN/1% TFA. The samples in 95% ACN/1% TFA were loaded to the cartridges and washed four times with 95% ACN/1% TFA. N-glycopeptides were eluted twice in 0.4 mL of 50% ACN/0.1% TFA and dried under nitrogen. The residue was then reconstituted in 30 μL of water ready for deglycosylation steps. The N-glycopeptides were deglycosylated by a combination of

endoglycosidases (endoF2, endoF3 and endoD). Specifically, the N-glycopeptides were dissolved in 1x GlycoBuffer and then treated with 5 μL of endoF2 (Sigma-Aldrich) and 5 μL endoF3 (Sigma-Aldrich) overnight at 37°C under agitation. The samples were dried under nitrogen and dissolved in 22 μL of water before adding 5 μL of endoD and Glycobuffer (BioLabs) with an overnight incubation at 37°C under agitation. The samples were prepared for nano LC/MS-MS analysis by desalting procedures with StageTip C18 (Thermo Fisher Scientific) and finally dissolved in 20 μL 10% formic acid. For the unbound fraction derived from LCA enrichment, the samples were subjected to OASIS MAX, endoF2/F3 and endoD deglycosylation as previously reported. Finally, the peptides were desalted using OASIS PRIME HLB C18 and resuspended in 150 μL of 10% formic acid. To identify and quantify core-fucosylated (GlcNAcFuc), non-fucosylated (GlcNAc), and unmodified peptides of N-glycoproteins desalted samples (3 μL injected) were analyzed on Q-Exactive mass spectrometer (Thermo Fisher Scientific) equipped with a nano-electrospray ion source (Proxeon Biosystems) and a nUPLC Easy nLC 1000 (Proxeon Biosystems). Peptide separations occurred on a homemade (75-μm i.d., 15-cm long) reverse phase silica capillary column, packed with 1.9-μm ReproSil-Pur 120 C18-AQ (Dr. Maisch GmbH, Germany). A gradient of eluents A (water with 0.1% formic acid) and B (ACN with 0.1% formic acid) was used to achieve separation (300 nL/min flow rate), from 2% to 40% B in 88 minutes. Full-scan spectra were acquired with the lock-mass option resolution set to 70,000 and mass range from m/z 300 to 2,000. The experiments were performed in technical triplicates. The 10 most intense doubly and triply charged ions were selected and fragmented. All MS/MS samples were analyzed using Mascot (version 2.6, Matrix Science) engine to search the human proteome 20201007 (42,358 sequences and 24,316,585 residues). Searches were performed with the following settings: Trypsin as proteolytic enzyme; 2 missed cleavages allowed; carbamidomethylation on cysteine as fixed modification; protein N-terminal-acetylation, methionine oxidation, GlcNAcFuc and GlcNAc as variable modifications; mass tolerance was set to 5 ppm and to 0.02 Da for precursor and fragment ions, respectively. To quantify proteins and to identify the core-fucosylated (GlcNAcFuc) and the non-fucosylated (GlcNAc) sites, the raw data were uploaded into the MaxQuant (RRID:SCR_014485) software version 1.6.1.0. Label-free protein quantification was based on the intensities of precursors. The intensity of each GlcNAcFuc peptide was normalized to the intensity of the originating protein. Statistical analysis and hierarchical clustering were performed by MeV software. The identified proteins were also analyzed by DAVID (RRID: SCR_001881) software to assess the cell compartment localization (GO_CC), the biological process (GO_BP), and the molecular function (GO_MF) in which the proteins were involved.

For WB analysis following the LCA affinity enrichment, each frozen cell pellet was first denatured in 0.5 mL of 8 mol/L urea in Tris HCl pH 7.6 with the addition of protease inhibitors (Halt Protease Inhibitor Cocktail; 100X; Thermo Fisher Scientific) and of phosphatase inhibitors (PhosStop, Merck), and then sonicated thoroughly for 3 minutes. Protein concentration was measured using a BCA protein assay kit (Thermo Fisher Scientific). One mg of total proteins was then reduced by incubation with 10 mmol/L DTT for 1 hour at 56°C and alkylated by addition of 27 mmol/L iodoacetamide at room temperature for 30 minutes in ABC 0.1 mol/L and then subjected to LCA affinity enrichment as detailed above.

Untargeted metabolomics on GBM xenografts

PN GSC- and MES GCL/GSC-derived xenografts ($n = 8$ from 3 distinct PN GSCs and $n = 8$ from 1 MES GCL line and 2 MES GSC

lines) were subjected to untargeted metabolomics (Metabolon). Samples were prepared using the automated MicroLab STAR system from Hamilton Company. Several recovery standards were added before the first step in the extraction process for QC purposes. To remove protein, to dissociate small molecules bound to protein or trapped in the precipitated protein matrix, and to recover chemically diverse metabolites, proteins were precipitated with methanol. The resulting extract was divided into five fractions: Two for analysis by two separate reverse-phase (RP)/UPLC/MS-MS methods with positive ion mode electrospray ionization (ESI), one for analysis by RP/UPLC/MS-MS with negative ion mode ESI, one for analysis by HILIC/UPLC/MS-MS with negative ion mode ESI, and one sample was reserved for backup. All methods used a Waters ACQUITY ultra-performance liquid chromatography (UPLC) and a Thermo Fisher Scientific Q-Exactive high resolution/accurate mass spectrometer interfaced with a heated ESI (HESI-II) source and Orbitrap mass analyzer operated at 35,000 mass resolution. Raw data were extracted, peak-identified, and QC processed using Metabolon's hardware and software. Peaks were quantified using AUC.

Radiosynthesis and quality control of 6-[^{18}F]fluoro-fucose PET tracer

6-deoxy-6-[18F]F-α-Lgalactopyranose precursor was purchased from ABX. Radiosynthesis of 6-[18F]Fluoro-Fucose (6-[18F]FFuc) was conducted in a GE TRACERlab FX-automated module. [^{18}F]Fluoride was produced via the 18O(p,n)18F nuclear reaction by irradiation of [18O]H2O water in a Niobium target (2 mL) using a 18 MeV cyclotron (18 Twin, IBA RadioPharma Solutions). The radionuclide was transferred from target in a water bolus by means of helium flow and trapped on a preconditioned Sep-pak Light QMA cartridge (ABX) to separate [^{18}O]H2O. [^{18}F]Fluoride was eluted with 1 mL of Kryptofix 2.2.2 in acetonitrile (20 mg/mL) and 0.5 mL of K2CO3 in water (6 mg/mL). After azeotropic distillation, the precursor 1,2,3,4-di-O-isopropylidene-6-(trifluoromethane-sulfonyl)oxy-L-galactose (8.5–10 mg), dissolved in 1 mL of acetonitrile, was added to the dried residue in the reaction vessel and heated to 85°C for 5 minutes. Hydrolysis of the fluorinated intermediate was achieved by addition of 1 mL of HCl 1N and heating at 80°C for 5 minutes. After quenching by addition of 3 mL of PBS 1 mol/L pH 7 the reaction mixture was purified passing through C18 light and Alumina N cartridges put in series. The product was collected and diluted with 5 mL of NaCl 0.9%. The injectable solution was passed through a sterilizing filter (0.20 μm) and collected into a sterile vial in a class A isolator. Not-decay corrected radiochemical yield was above 90%. Analytic HPLC Luna Omega 3 Sugar (Phenomenex) was used for determination of radiochemical purity. 6-[^{18}F]FFuc (4.3 minutes) and intermediate (3.2 minutes) were eluted with H2O/CH3CN 40:60 at 1 mL/min. Unlabeled [18F]Fluoride was assessed by radio-TLC on silica gel plate and H2O/CH3CN 5:95 as mobile phase. Radiochemical purity was above 99.9%. pH of the final solution was 6–7 by indicator strips. In-vial stability of 6-[^{18}F]FFuc was evaluated 4 hours after the end of the synthesis by HPLC and radio-TLC analysis and pH measurements. No loss of fluoride or sign of decomposition was observed in the storage conditions used and in the final formulation composition (phosphate/saline).

PET imaging

The potential use of 6-[^{18}F] fluoro-L-Fucose as radiopharmaceutical tracer was evaluated by CT/PET (X-ß-CUBE; Molecubes) in NSG female mice that received intracranial transplantation with three distinct MES GCL/GSC lines (L1312, L0420, and U87) and two PN

GSC lines (L0605 and L0125). PET studies were performed when the tumor volume as measured by T2-weighted MRI was at least 15 to 20 mm^3. Mice were anesthetized with isofluorane (2% in oxygen) and positioned on the CT scan. At the end of CT acquisition, 3.5–4.2 MBq of 6-[^{18}F]fluoro-L-Fucose were injected in the tail vein, the bed transferred from CT to the PET scan and the kinetics of radioactivity distribution acquired for 90 minutes according to the following protocol: 5 frames of 1 minute, 2 frames of 2.5 minutes, 4 frames of 5 minutes, 6 frames of 10 minutes. Images were reconstructed using the OSEM algorithm and corrected for 18F decay.

The kinetics of radioactivity distribution were calculated by manually drawing the volume of interest (VOI) in different body districts, including the tumor, the contralateral healthy brain parenchyma, heart, liver, and kidneys, using the PMOD 3.2 Software (RRID: SCR_016547). Brain regions were defined on co-registered MRI images and then copied on brain PET images. VOIs were centered on the striatum for normal brain parenchyma and on the MRI hyperintensity tumor signal for tumor lesions. Peripheral VOIs were defined on CT scans. Heart VOIs were drawn on the heart cavity to calculate blood time–activity curves (TAC). Radioactivity concentration values were expressed as the percentage of the injected dose per gram of tissue (%ID/g). To determine the kinetics of 6-[^{18}F]FF and to estimate tissue distribution volume (V_t) and V_t ratios between tumor and contralateral brain parenchyma, TACs curves from blood, contralateral healthy brain parenchyma, and tumors were used for graphical Logan analysis. Considering that tumors identified using MRI did not show homogenous 6-[^{18}F]FF uptake, VOIs corresponding to 50% of the maximum %ID/g value were defined using the *isocontour* tool in static brain PET images acquired between 60 and 90 minutes. To evaluate the potential use of static images to measure 6-[^{18}F]FF uptake in tumors, a correlation analysis was performed between V_t ratios derived from the Logan analysis on tumor and normal brain parenchyma and radioactivity concentration ratios calculated on the integral of frames obtained between 60 and 90 minutes from tracer injection.

To understand whether 6-[^{18}F]FF uptake was the result of tracer incorporation into tissue proteins (irreversible tracer) or was regulated by blood-to-tissue exchange (reversible tracer), a compartmental analysis was applied to dynamic PET kinetics data. In the irreversible trapping-compartment model, a tracer tissue distribution volume (Vt) of the reversible compartment is $Vt = k_1/(k_2 + k_3)$, whereas in the reversible non–trapping-compartment model (i.e., $k_3 = 0$) the distribution volume equation is $Vt = k_1/k_2$. K_1 denotes the transport rate constant from blood to tissue, k_2—the reverse of k_1—represents the rate constant of reversible transport from the tissue compartment back to blood, and k_3 represents the rate constant of tracer trapping (see Schematic Supplementary Methods S1).

Statistical analysis

All statistical analysis and plotting were performed with GraphPad Prism v9 (RRID:SCR_002798). Results for continuous variables were expressed as mean ± standard error of the mean. Two-group comparisons were performed with the Student t test (independent samples, one tail or two tails, 95% confidence interval). In cases of not-normal distribution, the non-parametric Mann–Whitney test (non-equal SD and not normal distribution, two tails) was used. Multiple group comparisons were performed with one-way ANOVA and/or two-way ANOVA followed by Tukey or Dunnett multiple comparison test. A P value of <0.05 was considered statistically significant. *, $P < 0.05$; **, $P < 0.01$; ***, $P < 0.005$; ****, $P < 0.001$.
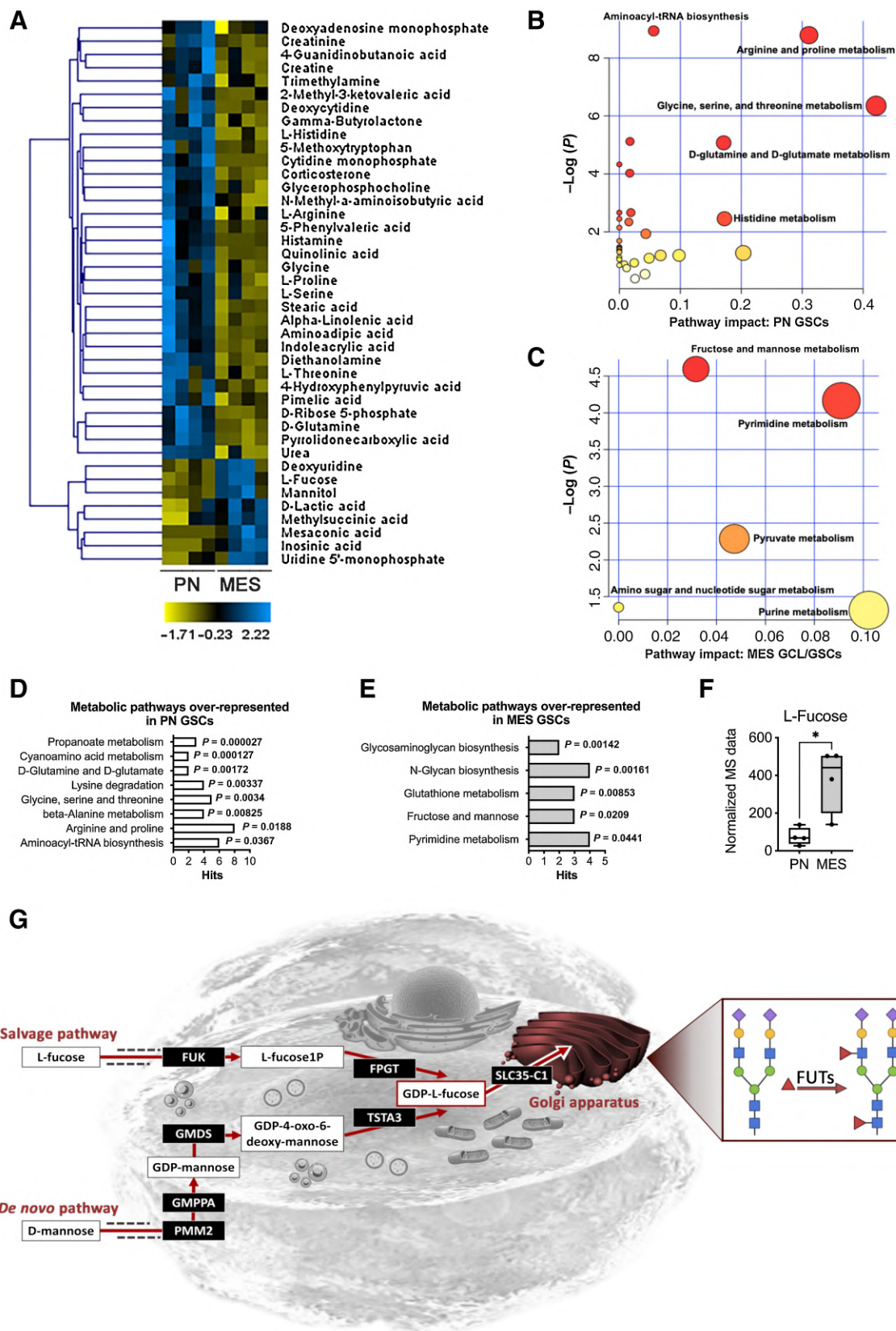
Figure 1.
Metabolomic and transcriptomic profiling of subgroup-specific GSCs identifies L-Fucose as a mesenchymal-restricted metabolite. **A,** Hierarchical clustering of differentially represented metabolites identified and quantified by LC/MS-MS analysis in PN and MES GSCs (peak area). Yellow, lowest abundance; blue, highest abundance. (*Continued on the following page.*)
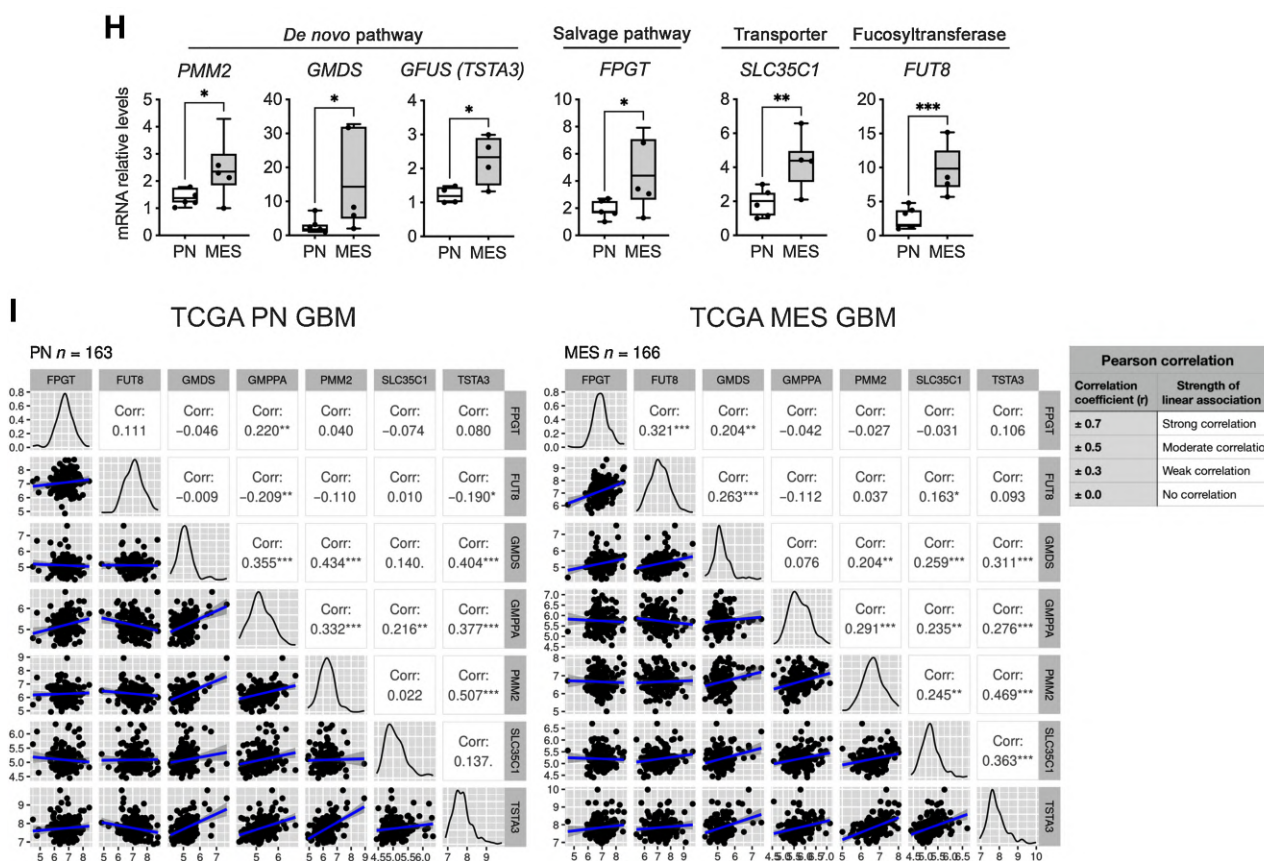
Figure 1.
(*Continued.*) **B** and **C,** Metabolic pathway analysis plots for PN and MES GSCs by MetaboAnalyst. The top pathways are ranked by the gamma-adjusted *P* values for permutation per pathway (*y*-axis) and the total number of hits per pathway (*x*-axis). The color grades from white to yellow, orange, and red as the values of both *x* and *y* axes increase. **D** and **E,** Integrated pathway analysis of transcriptomic and metabolomic data. The significantly enriched ($P < 0.05$, fold change > 1) genes from RNA-seq and metabolites from metabolomic analysis of PN and MES GSCs were integrated by combining a hypergeometric test for enrichment analysis and degree centrality in topology analysis based on gene-metabolite pathways using MetaboAnalyst. **F,** Normalized MS peak area of L-Fucose metabolite in PN and MES GSCs. Quantitative data are represented as a box-and-whisker plot, with bounds from 25th to 75th percentile, median line, and whiskers ranging from minimum to maximum values. Student *t* test, unpaired. **G,** Schematic representation of L-Fucose metabolic network depicting the contribution of both the *de novo* synthesis and the salvage pathways to GDP-fucose synthesis and the role of fucosyltransferases (FUT) in glycan fucosylation (created with BioRender.com). **H,** Several genes, encoding for critical enzymes in the L-Fucose metabolic pathway, are more highly expressed in MES than in PN GSCs (RT-qPCR). Quantitative data are represented as a box-and-whisker plot, with bounds from 25th to 75th percentile, median line, and whiskers ranging from minimum to maximum values. Student *t* test, unpaired. **I,** Pairwise Pearson correlation analysis of seven representative genes in L-Fucose synthesis pathway (TCGA dataset; Gliovis platform: http://gliovis.bioinfo.cnio.es). Plots indicate gene expression data from PN and MES GBM samples for *FPGT, FUT8, GMDS, GMMPA, PMM2, SLC35C1,* and *TSTA3*. Correlation coefficient (*R*) values and statistical significance are shown. *, $P < 0.05$; **, $P < 0.01$; ***, $P < 0.005$.

Data availability

The metabolomics data from GSCs generated in this study are publicly available at MetaboLights, project reference MTBLS4708, https://www.ebi.ac.uk/metabolights/MTBLS4708.

The mass spectrometry proteomics data generated in this study are publicly available at the ProteomeXchange Consortium via the PRIDE partner repository with the dataset identifier PXD033408 and DOI 10.6019/PXD033408.

The RNA-seq data generated in this study are publicly available at NCBI GEO (GEO accession number GSE202200).

The metabolomics data from GSC-derived xenografts generated in this study are publicly available at MetaboLights, project reference MTBLS730, https://www.ebi.ac.uk/metabolights/MTBLS730.

Results

Metabolomic and transcriptomic profiling of subgroup-specific GSCs identifies L-fucose as a MES-restricted metabolite

With the goal of pinpointing MES-restricted metabolic mediators (Supplementary Schematic S1), we subjected to LC/MS-based untargeted intracellular metabolomics 4 PN (L0627, L0605, L0306, and L0512) and 2 MES GSC lines (L1312 and L0315). All these GSC lines were generated through the NeuroSphere Assay (NSA) and were endowed with (i) short- and long-term self-renewal ability, (ii) expression of stem cell markers, (iii) multipotency, and (iv) tumorigenic potential (31, 33).

As internal controls for MES GBM cells, we added two commonly used GCLs (U87 and U251), which, although showing inherent

limitations in terms of fidelity to the tumor of origin (34), are transcriptionally classified as MES GBM cells and show exacerbated MES traits (31). Because the serum-containing conditions for GCLs may introduce substantial changes in the metabolome, we cultured MES GCLs for 48 hours in the NSA conditions after serum starvation.

Untargeted metabolomics data were subjected to PCA that, based on GSC metabolic profiles, identified two main clusters that well correlated with the molecular subgroup affiliation of each cell line (Supplementary Fig. S1).

The intracellular metabolic profiles of PN and MES GCLs/GSCs were further plotted in a hierarchical clustering to pinpoint metabolites that were differentially accumulated ($P < 0.05$). Forty-one out of the 201 metabolites identified from a library of 400 standard compounds were significantly different between PN and MES GCLs/GSCs, with 33 metabolites being accumulated in PN GSCs, and 8 in MES GCLs/GSCs (**Fig. 1A**). The list of differentially accumulated metabolites was then subjected to the "Pathway Analysis" module of MetaboAnalyst (35) to define the metabolic pathways in which the differentially expressed metabolites were involved. PN GSCs were enriched in pathways associated with glycolytic metabolism, the D-glutamine and D-glutamate metabolism, the glycine, serine, and threonine metabolism as well as in the arginine and proline metabolism (**Fig. 1B**). Conversely, MES GCLs/GSCs showed a significant enrichment in lactate production and enhanced purine and pyrimidine metabolism (**Fig. 1C**). Most notably, MES GCLs/GSCs were characterized by the activation of the fructose and mannose metabolism (**Fig. 1C**).

Next, we subjected the RNA-seq–based gene signatures distinguishing PN and MES GSCs that we previously reported (31) to an integrated bioinformatics analysis. By the "*Joint Pathway Analysis*" module of MetaboAnalyst, which matches the genes overexpressed with the metabolites enriched in the same subgroup of GSCs, PN GSCs were characterized by a statistically significant upregulation of KEGG global metabolic networks involved in propanoate metabolism, cyanoamino acid metabolism, aminoacyl-tRNA biosynthesis, as well as aminoacid metabolism (**Fig. 1D**). On the other hand, MES GSCs were predicted to activate glycosaminoglycan biosynthesis, N-Glycan biosynthesis, glutathione metabolism, fructose and mannose metabolism, and pyrimidine metabolism (**Fig. 1E**), thus confirming the enrichment of the same metabolic pathways, previously identified by metabolomics.

Most interestingly, the finding that the fructose and mannose metabolic pathway, the glycosaminoglycan biosynthesis pathway, and N-glycan biosynthesis pathway were all specifically enriched in MES GSCs suggested that L-Fucose, one of the metabolites significantly accumulated in MES GCLs/GSCs (**Fig. 1A** and **F**) and involved in all the above-mentioned pathways, could be a promising candidate metabolite for further characterization.

Thus, we assessed whether genes coding for critical enzymes involved in the L-Fucose synthesis/transport/conjugation pathways (**Fig. 1G**) were upregulated in MES versus PN GSCs (31). Of note, genes coding for many enzymes involved in L-Fucose biosynthesis, for example, *PMM2, GMPPA, GMDS,* and *FPGT,* were all significantly upregulated in MES GSCs (Supplementary Table S1A). Likewise, genes coding for enzymes needed for the synthesis of N-glycans and glycosaminoglycans, for example, *MAN1A1, B4GALT,* and *B3GNT2,* were again overexpressed in MES GSCs (Supplementary Table S1A). Most notably, among all the genes encoding for the different FUTs, only *FUT8* was significantly upregulated in MES GSCs (Supplementary Tables S1A and S1B). Accordingly, *in silico* analysis of expression data from the publicly available datasets GSE98995 (36) and GSE49161 (10), which comprise molecularly classified PN and MES GSC lines, indi-

cated that, notwithstanding the differences in GSC culturing conditions, most of the L-Fucose pathway genes showed a positive trend in expression in GSCs classified as MES (Supplementary Figs. S2A–S2C and S3A–S3C). We then *wet* validated the expression of these and other L-Fucose metabolism-related genes by qPCR in our own GCLs/GSCs and confirmed that most of them, including *FUT8,* were more highly expressed in MES GCLs/GSCs than in PN GSCs (**Fig. 1H**).

To test the clinical relevance of the activation of the L-Fucose pathway in patients with glioma, we analyzed the TCGA_GBMLGG dataset, which includes transcriptional information of gliomas with different histology and grade ($n = 667$; Gliovis platform: http://gliovis.bioinfo.cnio.es/; ref. 37). Of note, six out of seven L-fucose pathway genes were significantly more highly expressed in GBMs than in lower grade gliomas (Supplementary Fig. S4A and S4B), implying their involvement in progression from low- to high-grade disease. Accordingly, high expression of the same genes in all types of gliomas was associated with a significantly worse prognosis (Supplementary Fig. S4C).

To analyze the correlation in the expression of L-Fucose pathway genes in the different GBM patients' subgroups, we assessed their expression pattern in GBM samples from the TCGA GBM dataset (**Fig. 1I**) and others (Supplementary Fig. S4D; ref. 38). Remarkably, the expression of these genes more significantly and positively correlated with one another in MES ($n = 163$) than in PN GBM samples ($n = 166$; **Fig. 1I**), indicating that the coordinated regulation of genes involved in the L-Fucose pathway takes place specifically in MES GBMs.

Next, by the Single-Cell Portal (https://singlecell.broadinstitute.org/single_cell), we analyzed the expression of the same genes in the scRNA-seq dataset SCP503 (27) and found out that, as observed for known MES-specific gene classifiers, L-Fucose–related genes were more highly expressed in single cells that were classified as MES based on MES-specific gene signatures (Supplementary Fig. S5A–S5C).

Enhanced FUT8 protein accumulation and core fucosylation are retrieved specifically in MES GSCs, in their corresponding xenografts and in MES GBM human specimens

Among L-Fucose pathway genes, we focused our interest on *FUT8,* which was the only FUTs significantly upregulated in our MES GSCs (Supplementary Table S1A and S1B). In agreement with the results from the transcriptional analysis and qPCR, FUT8 protein was more highly abundant in MES than in PN GSCs ($n = 4$ each; **Fig. 2A**). Because FUT8 specifically mediates core fucosylation, we also assessed the overall core fucosylation levels in the same GSCs by the core fucosylation-specific lectin AAL. MES GSCs were again characterized by a higher core fucosylation status than PN GSCs (**Fig. 2A**). The same difference was observed by AAL IF on PN and MES GSCs (**Fig. 2B**), and it was particularly evident when GSCs were not permeabilized, suggesting that most MES-specific core-fucosylated target proteins might reside on the cell membrane.

To assess the potential involvement of FUT8 in modulating the malignancy of MES GBMs *in vivo,* we analyzed by IHC (i) xenografts generated by the orthotopic transplantation of PN and MES GSCs, (ii) a cohort of molecularly classified human GBM specimens ($n = 5$ samples for each GBM transcriptional subgroup; ref. 29), and (iii) adult healthy brain specimens as controls ($n = 3$ samples). Again, FUT8 protein was restricted to MES GBMs (**Fig. 2C** and **D**; Supplementary Fig. S6A). In line with these findings, tumor cells in MES xenografts were endowed with higher core fucosylation in their cytoplasm than tumor cells in PN xenografts (**Fig. 2E**). Remarkably, the same pattern of AAL staining was detected in human MES GBM samples when compared with PN ones (**Fig. 2E**).
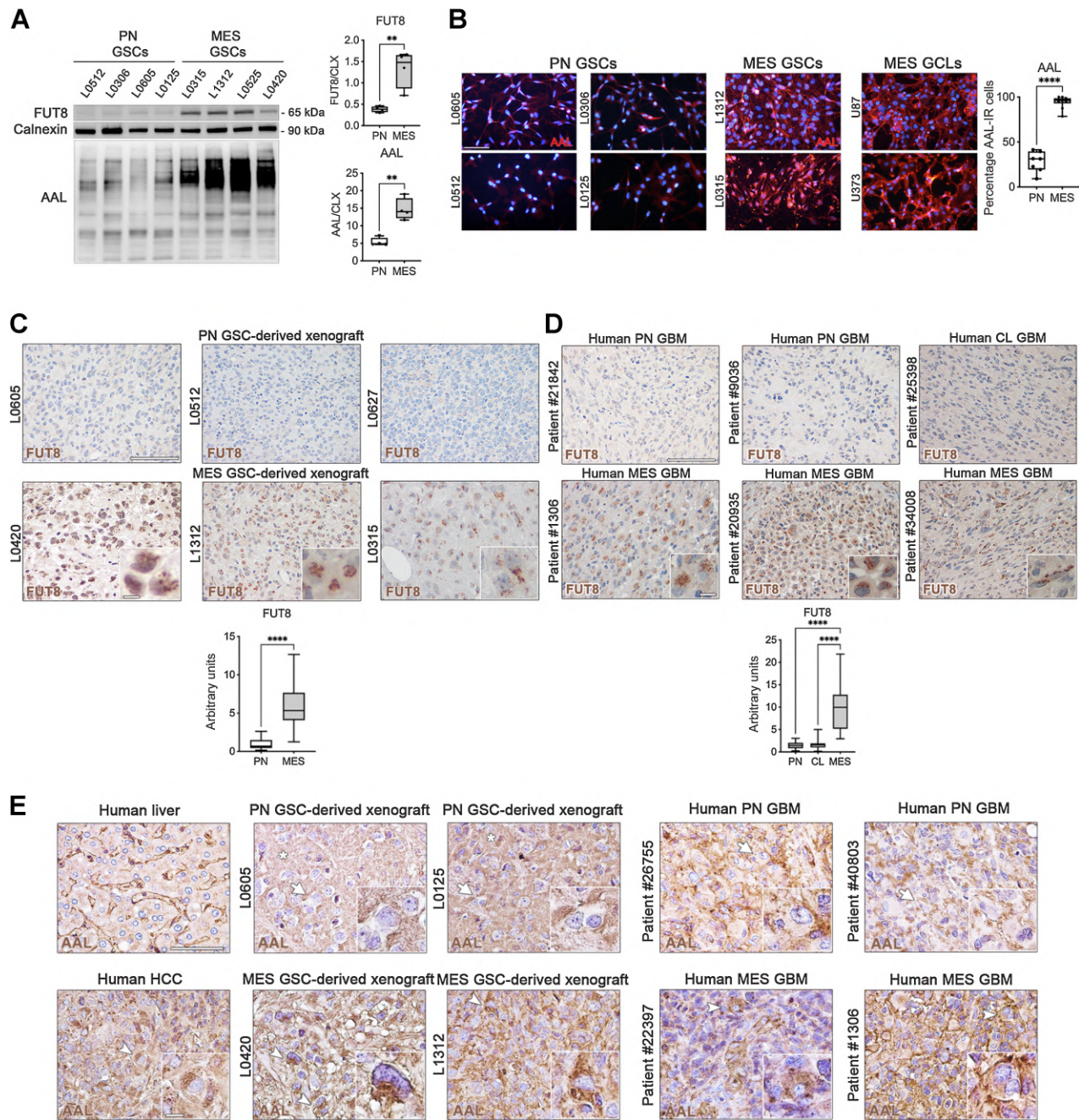
Figure 2.
Enhanced FUT8 protein accumulation and core fucosylation are retrieved specifically in MES GSCs, in their corresponding xenografts and in MES GBM human specimens. **A,** FUT8 protein abundance and core fucosylation, as measured by Aleuria Aurantia Lectin (AAL) blotting, are higher in MES GSCs than in PN GSCs (WB). Calnexin (CLX) is used as normalizer. Quantitative data are represented as box-and-whisker plots, with bounds from 25th to 75th percentile, median line, and whiskers ranging from minimum to maximum values. Student t test, unpaired. **B,** Immunofluorescence staining for AAL (red) shows increased core fucosylation in MES GSCs, when compared with PN GSCs. DAPI nuclear counterstaining, blue. Scale bar, 50 μm. Quantitative data are represented as a box-and-whisker plot, with bounds from 25th to 75th percentile, median line, and whiskers ranging from minimum to maximum values. Student t test, unpaired. **C,** FUT8-immunoreactive (-IR) cells (cytoplasmic staining, brown) were detected in MES GSC-derived intracranial xenografts. Quantification of FUT8 expression in the same xenografts ($n = 5$ different xenografts for each subgroup of GSCs). Scale bars, 50 μm; insets, 10 μm. Quantitative data are represented as box-and-whisker plots, with bounds from 25th to 75th percentile, median line, and whiskers ranging from minimum to maximum values. Student t test, unpaired. **D,** FUT8-IR cells (cytoplasmic staining, brown) were observed only in human MES GBMs. Scale bars, 50 μm; insets, 10 μm. Quantification of FUT8 expression in the same specimens ($n = 5$ different specimens for each subgroup of GBM). Quantitative data are represented as box-and-whisker plots, with bounds from 25th to 75th percentile, median line, and whiskers ranging from minimum to maximum values. One-way ANOVA followed by a Tukey multiple comparison test. **E,** Specific staining for AALs (cytoplasmic, brown) was found in the cytoplasm of most tumor cells in MES GCL/GSC-derived intracranial xenografts and in human MES GBMs (white arrowheads; insets), whereas it is never detected in tumor cells in PN GSC-derived intracranial xenografts and human PN GBMs (white arrows; insets). In PN xenografts, AAL staining is observed only in the mouse brain neuropil (asterisk). Human liver, negative control. Human hepatocellular carcinoma (HCC), positive control. Scale bars, 50 μm; insets, 10 μm. **, $P < 0.01$; ****, $P < 0.001$.
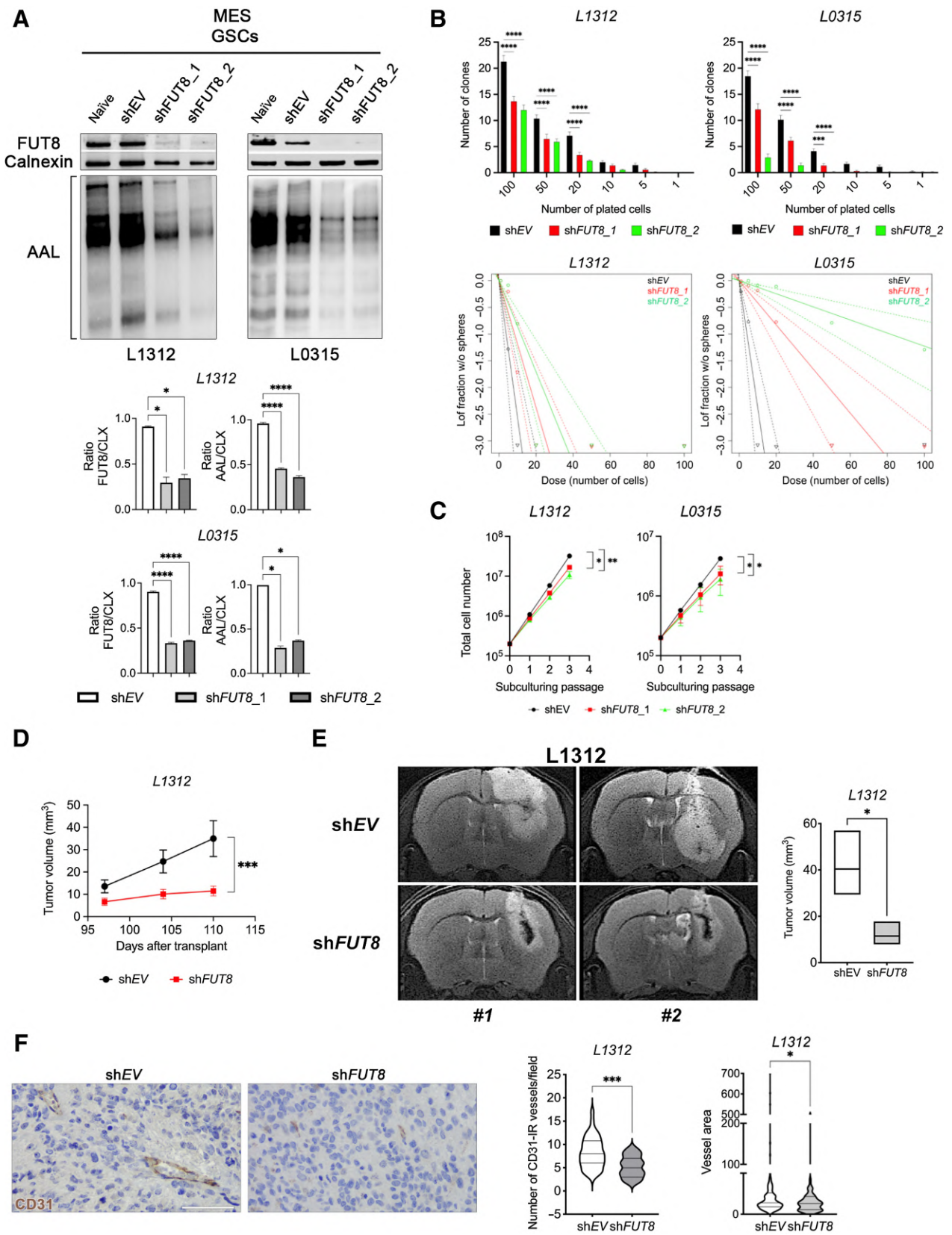
Therefore, the expression and activation of mediators of the L-fucose metabolism at the protein level may serve as potentially exploitable diagnostic biomarkers for MES GBMs.

FUT8 silencing impairs self-renewal and frequency of MES GSCs, reduces their core fucosylation, and decreases the growth of orthotopic MES GBM xenografts

To dissect the function of FUT8-mediated core fucosylation in MES GCLs/GSCs, we silenced FUT8 by means of 2 different lentiviral short hairpin (sh)RNA clones in MES GCLs (U87) and MES GSCs (L1312 and L0315). FUT8 silencing, as confirmed by significant reduction in FUT8 protein levels by WB (Fig. 3A; Supplementary Fig. S7A), induced a strong decrease in the core fucosylation of all the three MES GCL/GSC lines (Fig. 3A; Supplementary Fig. S7A) and a significant reduction in their short-term self-renewal, sphere-forming cell frequency, and long-term self-renewal, as measured by clonogenic assays, extreme limiting dilution analysis (Fig. 3B), and population analysis at different subculturing passages (Fig. 3C; Supplementary Fig. S7B). Moreover, FUT8 silencing significantly decreased the expression of GMDS and GMPPA, which are both part of the de novo L-Fucose synthesis pathway (Supplementary Fig. S7C).

Most relevantly, FUT8 knockdown consistently impaired the growth of MES GCL/GSC-derived orthotopic xenografts, as assessed by 7 Tesla T2-weighted (T2w) MRI-based volumetric longitudinal analysis (Fig. 3D and E; Supplementary Fig. S7D).

Because tumor neo-angiogenesis is regulated by core fucosylation (39), we analyzed FUT8-silenced xenografts by IHC for the vessel marker CD31. Notably, the extent of angiogenesis by counting CD31-IR vessels and measuring their area was significantly decreased in FUT8-silenced GCL/GSC-derived xenografts as compared with controls (Fig. 3F; Supplementary Fig. S7E).

Treatment with the fucose-analogue 2FF hampers MES GCL/GSC core fucosylation and proliferation in vitro and inhibits their growth in vivo

Inhibitors of fucosylation have shown efficacy when tested in vitro and in vivo in liver and breast cancer models (40–42). Thus, we tested the anti-neoplastic activity of one of these inhibitors, that is, 2FF, in MES GCLs/GSCs in vitro and after their orthotopic transplantation in vivo. 2FF is a specific fluorinated analog of L-Fucose that enters cells via passive diffusion and is metabolized into the corresponding donor substrate analog of GDP-fucose, GDP-2FF, via the salvage pathway.

Dose-escalation experiments indicated that treatment with 2FF for 72 hours reduced global core fucosylation of MES GCL/GSC lines already at 25 µmol/L, achieving maximum efficacy at 100 µmol/L (Fig. 4A; Supplementary Fig. S8A). For survival studies, we tested 2FF at the same 100 µmol/L dose (Supplementary Fig. S8B), and at a 5-fold higher dose (500 µmol/L), to identify the highest dose that did not elicit off-target effects, as determined in PN GSCs. The maximum treatment efficacy in terms of impaired survival was achieved at 500 µmol/L in MES GCL/GSCs both at 48 and 72 hours (Fig. 4B; Supplementary Fig. S8C), while being ineffective in PN GSCs (Fig. 4B), further supporting the hypothesis that fucosylation may be a specific druggable vulnerability of MES GBMs.

To ensure effective and constant release of 2FF into the tumor and to avoid potential systemic toxic effects, we tested its activity in MES xenografts by exploiting an intratumor delivery strategy that mimicked convection enhanced delivery (CED). CED is used clinically to inject drugs, bypassing the blood–brain barrier in a targeted manner, thus resulting in therapeutically meaningful drug concentrations locally (43). We implanted Alzet osmotic minipumps subcutaneously and connected them to a brain-infusion kit that allowed effective local distribution of the drug (Supplementary Fig. S8D). Details about pump type, infusion rate, drug concentration, and daily doses are available in Supplementary Table S2. The initial drug concentration to be delivered intracranially was calculated by using 1/50 of the dose delivered orally reported in (40).

Xenografts derived from Luciferase (Luc)-transduced MES GCLs (U87) and GSCs (L1312) were treated by two different delivery schedules, to replicate different clinical settings. In both cases, local treatment did not result in any change in total body weight, locomotion, posture, and any other health indicator.

For GCL-derived xenografts (U87), treatment with 2FF started concomitant with intracranial cell transplantation, that is, before tumor development, thus reproducing a minimal residual disease clinical scenario. Tumor growth was monitored by 4 BLI scans acquired between days 2 and 14. T2w MRI analysis was performed at the end of the experiment (day 16; Supplementary Fig. S8E). U87-derived tumors were treated with vehicle or with a 1.6 mmol/L dose of 2FF (Supplementary Fig. S8E) that was further increased to 4 mmol/L (Supplementary Fig. S9A and S9B) to enhance efficacy. In both experiments, vehicle and 2FF were delivered at 0.25 µL/h for 16 days (n = 5 mice per condition/dose). A statistically significant volume reduction was observed in all tumors treated with either dose of 2FF, considering both the ratios of final/initial luciferase average radiance and the final volume measured by MRI (Supplementary Figs. S8E and

---

Figure 3.
FUT8 silencing impairs self-renewal and frequency of MES GSCs, reduces their core fucosylation, and decreases the growth of orthotopic MES GBM xenografts. **A,** Efficient silencing of FUT8 in MES GSC lines by distinct shRNA clones (shFUT8) results in decreased core fucosylation, as assessed by WB for AAL. Controls are defined as shEmpty Vector (shEV). Quantitative data are represented as bar graphs. Two-way ANOVA followed by a Tukey multiple comparison test. **B,** In vitro limiting dilution clonogenic assays (top) and extreme limiting dilution assays (ELDA; bottom) both indicate that knockdown of FUT8 in MES GSCs (L1312 and L0315) significantly decreases the frequency of GBM spheres. Quantitative data are means ± SEM (n = 12) and are represented as bar graphs. Two-way ANOVA followed by a Dunnett multiple comparison test. Sphere-forming cell frequencies by ELDA analysis: L1312, shEV 1/3.91; shFUT8_1 1/8.43; shFUT8_2 1/11.73; L0315, shEV 1/4.22; shFUT8_1 1/22.68; shFUT8_2 1/81.46. Pairwise test for differences in sphere-forming cell frequencies by ELDA analysis: L1312, shEV versus shFUT8_1 P = 0.0262; shEV versus shFUT8_2 P = 0.00137; L0315, shEV versus shFUT8_1 P = 3.95e-07; shEV versus shFUT8_2 P = 5.28e-19. **C,** Reduced expression of FUT8 negatively affects MES GSC long-term self-renewal as assessed by population analysis at different subculturing passages. Simple linear regression test. **D,** A significant delay in tumor growth is detected in FUT8-silenced MES GSC-derived xenografts (L1312), as monitored longitudinally by T2-weighted MRI up to 100 days. Simple linear regression test. **E,** Tumor volume is significantly reduced by FUT8 silencing in MES GSCs (L1312), as measured 100 days after transplantation (T2-weighted MRI; n = 4 different xenografts for each group). Student t test, unpaired. Quantitative data are represented as box-and-whisker plots, with bounds from 25th to 75th percentile, median line, and whiskers ranging from minimum to maximum values. **F,** The extent of tumor neo-angiogenesis, as measured by the number of vessels positive for CD31 in a ×20 microscopic field (cytoplasmic staining, brown) and their area, is negatively affected by inhibition of core fucosylation through FUT8 silencing. Hematoxylin was used as nuclear counterstaining (blue). Scale bar, 50 µm. Quantitative data are represented as violin plots. Mann–Whitney test, unpaired. *, P < 0.05; **, P < 0.01; ***, P < 0.005; ****, P < 0.001.

A MES GSCs

B Survival of MES GCLs/GSCs | Survival of PN GSCs

C

D

E
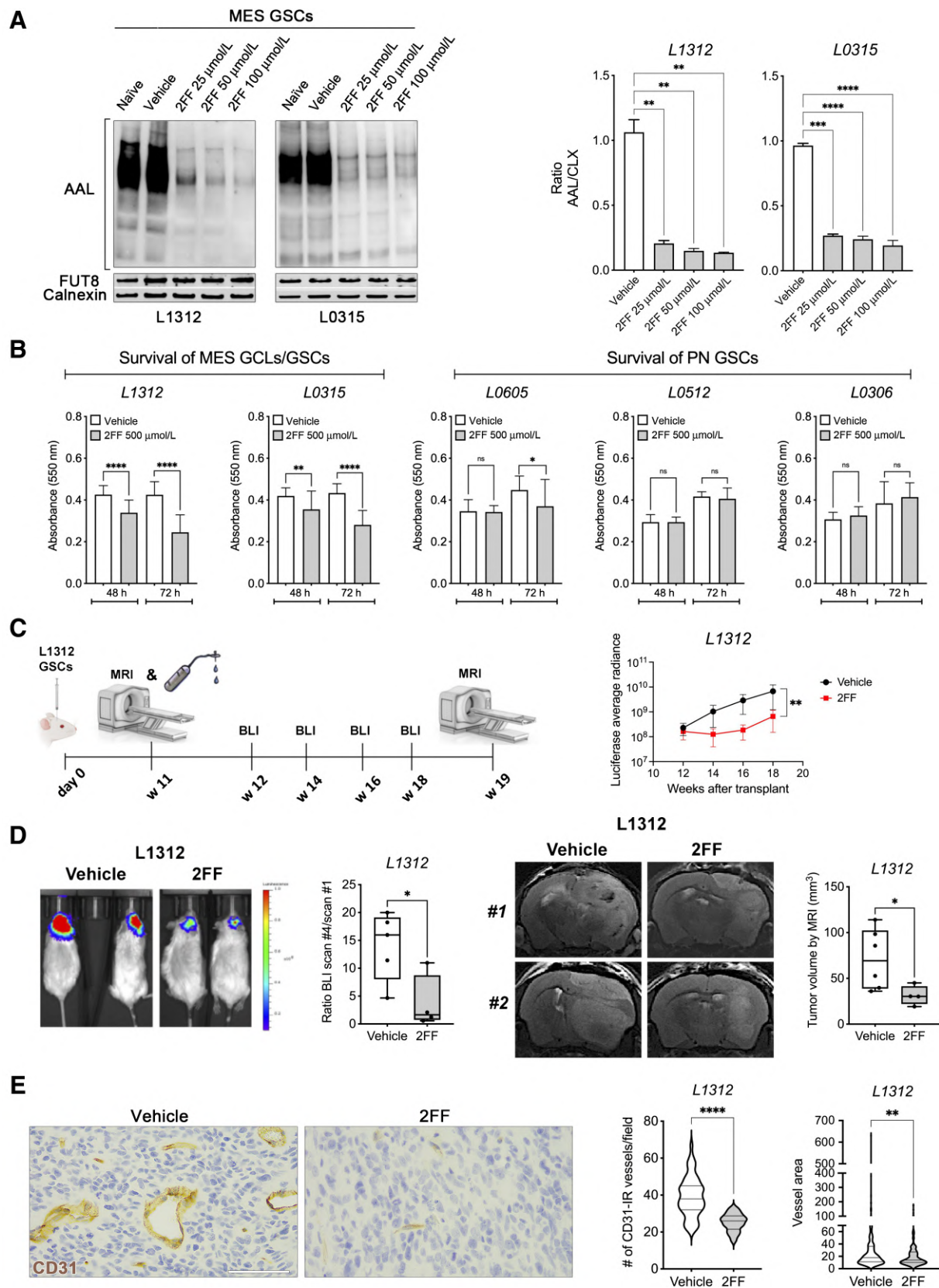
S9B), as well as a significant decrease in neo-angiogenesis (Supplementary Fig. S9C).

For MES GSC-derived xenografts (L1312), treatment started 11 weeks after transplantation, when tumors were clearly detectable by MRI, thus mimicking an unresectable tumor clinical setting. Mice with an average MRI-based tumor volume of 1.949 $\pm$ 0.716 mm^3 were randomized into two groups (Supplementary Fig. S9D) and implanted with osmotic pumps loaded with either vehicle or 6.6 mmol/L 2FF, both delivered at 0.15 μL/h for 6 weeks (**Fig. 4C**). Tumor growth was monitored by a longitudinal analysis based on 4 BLI scans taken between weeks 12 and 18 (**Fig. 4C**) and the final tumor volume measured by MRI at week 19 (**Fig. 4D**). Even in this case, 2FF-treated tumors were significantly smaller that the controls (**Fig. 4D**).

As observed in *FUT8*-silenced MES xenografts (**Fig. 3**), tumor neo-angiogenesis was again significantly impaired by 2FF treatment (**Fig. 4E**).

The expression of key enzymes of L-fucose pathway is transcriptionally regulated by the PN classifier ASCL1 during PN-to-MES transition

To identify the mechanism(s) by which FUT8 expression and core fucosylation are specifically increased in MES GBM, we assessed the involvement of known mediators of the PN-to-MES transition (PMT), such as Achaete-scute homolog 1 gene (*ASCL1*; refs. 31, 44). Silencing of *ASCL1* in PN GSCs is known to promote the acquisition of MES traits, by increasing the expression of MES gene classifiers (e.g., NDRG1), with a concurrent decrease in PN features (31).

To test whether also FUT8 expression was regulated by ASCL1, we assessed its protein accumulation *in vitro* in *ASCL1*-silenced PN GSCs (L0627; ref. 31), before and after reintroduction of *ASCL1*. Interestingly, knockdown of *ASCL1* in PN GSCs induced a significant increase in FUT8 protein abundance that was reverted to the original control level by *ASCL1* overexpression (**Fig. 5A**; Supplementary Fig. S10A and S10B). Notably, ASCL1-induced changes in FUT8 level were accompanied by the concomitant modulation of core fucosylation (**Fig. 5A**). We also assessed whether ASCL1 elicited the same repressive activity on FUT8 level in MES GSCs and this proved to be the case, with FUT8 expression being significantly reduced after *ASCL1* overexpression (**Fig. 5B**). To assess whether the regulation of FUT8 expression by ASCL1 could be detected in the absence of any genetic manipulation, we took advantage of a MES GBM postsurgery specimen that, when cultured *in vitro* under the NSA conditions, gave rise to a GSC line that progressively acquired PN features while decreasing MES traits (10, 36, 45). Notably, concurrent with the increased expression of ASCL1, we observed a significant decrease in the expression not only of the MES gene classifier NDRG1 but also of FUT8 (**Fig. 5C**),

further corroborating the critical role of ASCL1 in modulating FUT8 expression.

We previously reported that *ASCL1* silencing *in vivo* mimic PMT, by inducing the upregulation of MES gene classifiers and the acquisition of histomorphological MES features, such as the presence of large, spindle-shaped pleomorphic cells, organized in typical bundles (31). To test whether FUT8 might also be involved in the ASCL1-mediated PMT *in vivo*, we evaluated its abundance in *ASCL1*-silenced PN xenografts. Notably, downregulation of ASCL1 resulted in PMT, as well as in enhanced FUT8 expression and increased core fucosylation (**Fig. 5D**), indicating that FUT8 expression and FUT8-dependent core fucosylation may be associated with the acquisition of MES traits, and that FUT8 may be a direct transcriptional target of ASCL1.

To understand whether *FUT8* and other genes of the L-Fucose pathway, such as *GMDS* and *FPGT*, were direct targets of ASCL1, we performed ChIP–qPCR analysis on PN GSCs that expressed *ASCL1* either endogenously or ectopically. We designed ChIP–qPCR primers by testing regions comprising a putative ASCL1-binding site and a ChIP-seq peak, conserved among publicly available datasets of GBM (46) and other tumors (refs. 47, 48; **Fig. 5E**). We tested *EGFR* and *DKK1* genes as target and non-target controls, respectively (ref. 31; Supplementary Fig. S10C). *FUT8*, *GMDS*, and *FPGT* were confirmed to be direct targets of ASCL1, with all three genes bound by either endogenous or ectopic ASCL1 on their promoter region (**Fig. 5F**).

Altogether, these data indicate that (i) ASCL1 directly represses the expression of *FUT8, GMDS*, and *FPGT*, thus proposing them as potential MES markers that are derepressed during ASCL1-mediated PMT, and (ii) ASCL1 downregulation is one of the key mechanisms responsible for the restricted activation of the L-Fucose pathway in MES GBMs.

Core-fucosylated glycoproteins are enriched in MES GSCs and are involved in biological processes relevant for the MES phenotype

To investigate whether protein core fucosylation profiling could discriminate PN from MES GBM and to identify MES-restricted core-fucosylated proteins, we performed a MS-based glycoproteomic screening for site-specific core fucosylation in (i) PN GSC lines, (ii) MES GCL/GSC lines, and (iii) the same MES GCL/GSC lines after treatment with the fucosylation inhibitor 2FF ($n = 3$ cell lines for each condition). N-glycopeptides were enriched by LCA binding and then deglycosylated by a combination of endoglycosidases (endoF2, endoF3, and endoD) to identify core-fucosylated (HexNAcdHex), non-fucosylated (HexNAc), and unmodified glycopeptides. A total of 2,708 proteins were identified and quantified by label free approach; 108 HexNAcdHex total sites were identified, with 73 core

Figure 4.
Treatment with the fucose-analogue 2FF hampers MES GSC core fucosylation and proliferation *in vitro* and inhibits their growth *in vivo*. **A,** Core fucosylation of MES GSCs is significantly inhibited by treatment with 2FF for 72 hours. Quantitative data are represented as bar graphs. Two-way ANOVA followed by a Tukey multiple comparison test. **B,** Treatment with 500 μmol/L 2FF for up to 72 hours negatively impacts on the survival of MES GSCs, while being ineffective in PN GSCs. MTT assay. Quantitative data are represented as bar graphs. Student *t* test, unpaired. **C,** A significant delay in tumor growth is observed in established MES GSC-derived xenografts (L1312), which were implanted with osmotic pumps loaded with 6.6 mmol/L 2FF 11 weeks after transplantation and monitored longitudinally by BLI up to 18 weeks ($n = 5$ mice per condition; created with BioRender.com). Simple linear regression test. **D,** Tumor growth was assessed by BLI as the ratio between tumor total photons flux (p/s) at the last scan and at the first scan (mean ratio $\pm$ SEM: 14.06$\pm$2.75 for vehicle and 3.70$\pm$2.43 for 2FF). Tumor volume by MRI was measured as the tumor volume at the last time-point of analysis (19 weeks; mean volume $\pm$ SEM: 71.09$\pm$13.37 mm^3 for vehicle and 31.21$\pm$5.20 mm^3 for 2FF). Quantitative data are represented as a box-and-whisker plot, with bounds from 25th to 75th percentile, median line, and whiskers ranging from minimum to maximum values. Student *t* test, unpaired. **E,** Tumor neo-angiogenesis, as measured by the number of vessels positive for CD31 in a ×20 microscopic field (cytoplasmic staining, brown) and their area is negatively affected by inhibition of core fucosylation by 2FF administration. Hematoxylin was used as nuclear counterstaining (blue). Scale bar, 50 μm. Quantitative data are represented as violin plots. Mann–Whitney test, unpaired. *, $P < 0.05$; **, $P < 0.01$; ***, $P < 0.005$; ****, $P < 0.001$.
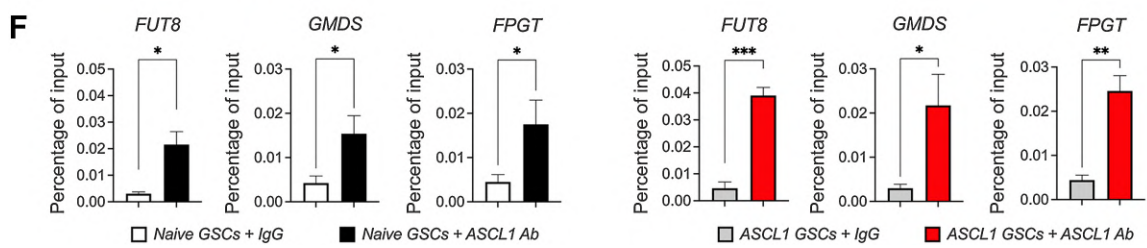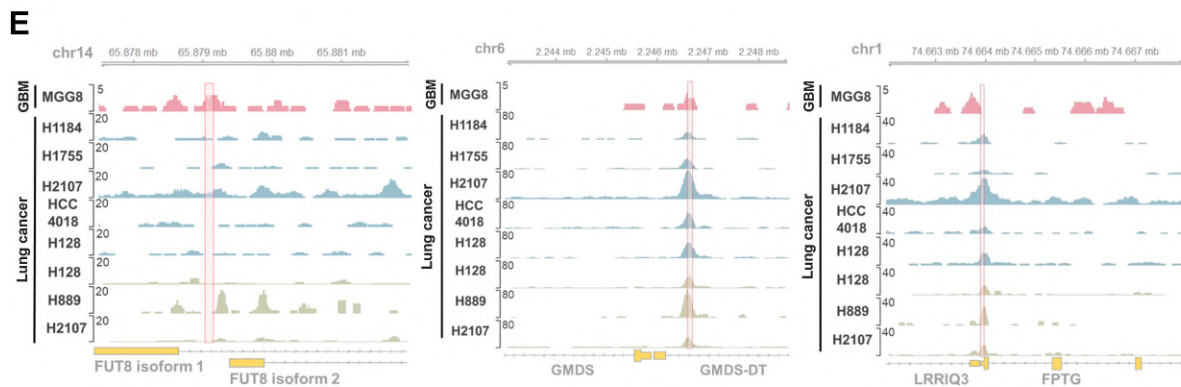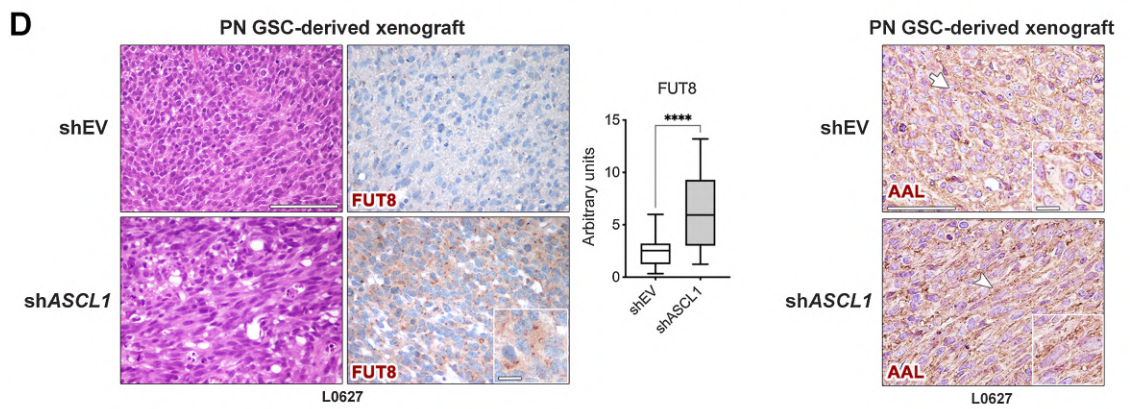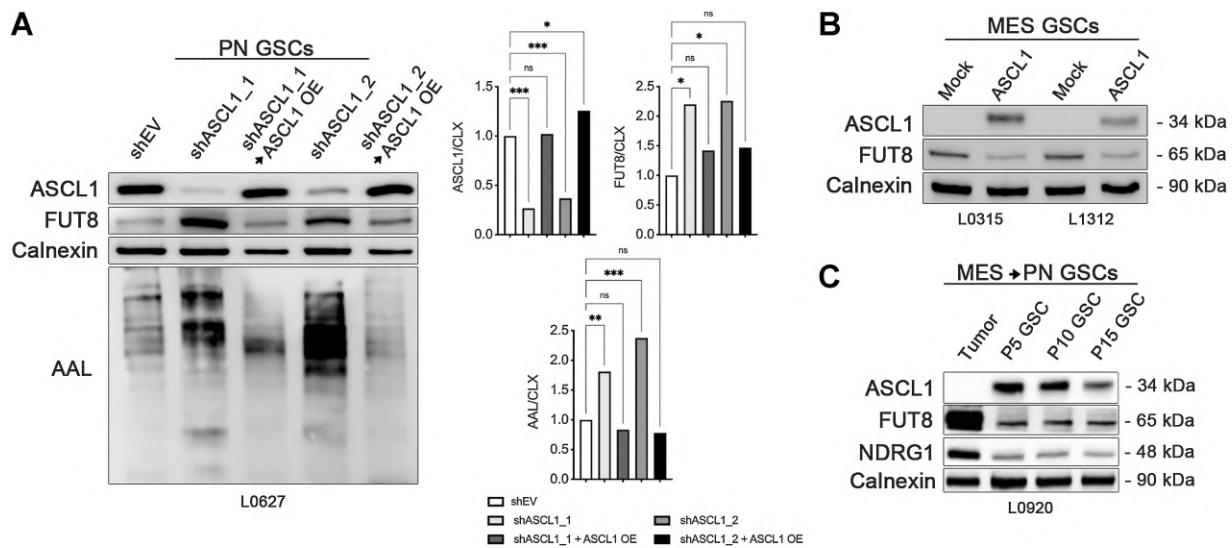
fucosylation-specific sites, containing the NXS/T consensus sequence, found in 54 different proteins. An example of MS/MS spectrum for the triply charged precursor at m/z 756.98 is shown in Supplementary Fig. S11.

On the basis of the 73 core-fucosylated sites, unsupervised clustering analysis identified 3 distinct groups of samples, with MES GSCs being separated from PN GSCs and from the same MES GSCs, whose core fucosylation was inhibited by 2FF (**Fig. 6A**). Thus, subgroup-specific GSC lines can be stratified according to different protein core fucosylation levels.

Out of 73 core-fucosylated sites, 24 were significantly differentially represented between all PN GSCs and all MES GCLs/GSCs and showed reduced fucosylation upon 2FF treatment (**Fig. 6B**). Gene ontology analysis by EnrichR performed on the 23 core-fucosylated proteins, containing the 24 significantly different core-fucosylated sites, indicated enrichment in extracellular matrix (ECM) organization and disassembly, cell adhesion, and integrin-mediated signaling pathway, which are all closely associated with the malignant phenotype of MES GBMs (ref. 17; **Fig. 6C**). Accordingly, several of these proteins are involved in ECM organization and cell adhesion, for example, basigin, integrin alpha-3 (ITGA3), integrin alpha-V, and intercellular adhesion molecule 1. Other core-fucosylated proteins are related to lysosomal function, for example, mannose-6-phosphate receptor (M6PR), and to MES features, for example, sortilin (SORT1) and CD44.

To *wet* validate the robustness of the glycoproteomic analysis, we selected ITGA3 and CD44, given that their core fucosylation was significantly reduced by 2FF in the MS-based glycoproteomic screen, as shown by the quantification of the corresponding HexNAcdHex-containing glycopeptides (**Fig. 6D**), and their coding genes were overexpressed in MES GSCs by RNA-seq (ITGA3 expression in MES vs. PN GSCs: log2 FC 2.1, $P_{adj} < 0.04$; CD44 expression in MES vs. PN GSCs: $\log_2$ FC 2.3, $P_{adj} < 0.0001$). We first tested ITGA3 and CD44 abundance in PN GSCs and MES GCLs/GSCs by WB and in their corresponding xenografts by IHC and confirmed that they were both upregulated in MES GCLs/GSCs and in MES xenografts (**Fig. 6E** and **F**).

Next, we performed LCA enrichment of total proteins in MES GCLs/GSCs that were treated or not with 2FF and then subjected LCA-enriched and no LCA-enriched (input) protein fractions to WB for ITGA3 and CD44. Notably, WB analysis showed reduced accumulation of both proteins in the LCA-enriched protein fractions obtained from 2FF-treated MES GCLs/GSCs, consistent with lower glycosylation on the two proteins and, in particular, lower core fucosylation due to the specific inhibition of the process by 2FF. Accordingly, no

differences in the abundance of the same proteins were detected in the absence of LCA enrichment after 2FF treatment. Thus, ITGA3 and CD44 proteins were confirmed as being MES-specific core-fucosylated proteins (**Fig. 6G**).

Many of the proteins that we identified as being core fucosylated in MES GSCs, including the integrin ITGA3 and the glycocalyx-mediator CD44, are known to tune the interaction with the ECM, thereby potentially linking core fucosylation with the acquisition of pro-migratory features in GBM. To test this hypothesis, we first assessed the direct role of *FUT8* in mediating the core fucosylation of ITGA3 and CD44, by performing LCA enrichment of total proteins in MES GSCs after *FUT8* silencing. In agreement with the results obtained by inhibiting core fucosylation by 2FF (**Fig. 6G**), the accumulation of both ITGA3 and CD44 proteins was significantly impaired in the LCA-enriched protein fraction obtained from *FUT8*-silenced MES GSCs (**Fig. 6H**), thus implying that both ITGA3 and CD44 are direct target proteins of *FUT8*.

Next, to test the collective migratory ability of the same *FUT8*-silenced MES GSCs, we subjected them to time-lapse 2D wound-healing assays that showed a significantly impaired migration of *FUT8*-silenced MES GSCs, as measured by their reduced capacity to fill the wound over 72 hours (**Fig. 6I**). Overall, our data suggest that core fucosylation of integrins and other ECM interactors by FUT8 may act as a key mediator of MES GBM promigratory features.

Minimally invasive imaging detection of L-Fucose accumulation in MES xenografts by preclinical PET

To assess whether MES GBMs that hyperactivate the L-Fucose pathway and are potentially vulnerable to treatment with 2FF could be identified by a minimally invasive imaging modality such as PET, we first investigated whether L-Fucose or one of its metabolites accumulated selectively in MES xenografts. To this end, we performed a comprehensive untargeted metabolomic analysis of intracranial xenografts derived from PN GSCs and MES GCLs/GSCs ($n = 3$ GCL/GSC lines for each subtype, with 3 biological replicates for each cell line) by comparison with a library of 3,300 standard metabolites.

PCA analysis indicated that the two subtypes of GBM xenografts clustered separately (Supplementary Fig. S12). Supervised comparison of the two groups identified 260 out of 789 detected metabolites that were differentially accumulated in PN versus MES xenografts (**Fig. 7A**). Metabolic pathway–enrichment analysis revealed that the metabolites present in either PN or MES xenografts were enriched in distinct pathways (**Fig. 7B**). In agreement with the finding that the global metabolism of tumor cells *in vitro* is different than that of the
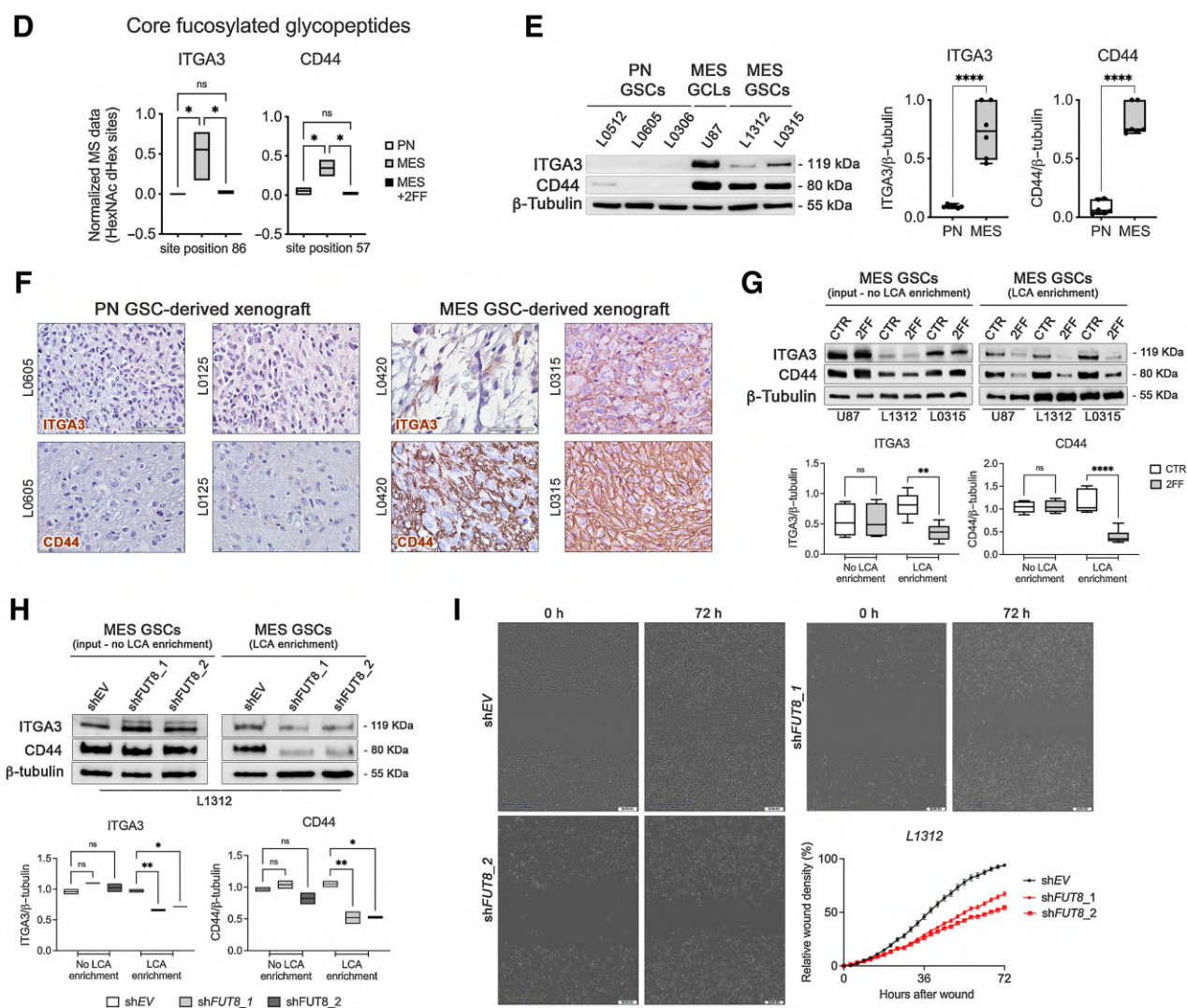
Figure 5.
The expression of key enzymes of the L-Fucose pathway is transcriptionally regulated by the PN classifier ASCL1 during PN-to-MES transition. **A,** Silencing of *ASCL1* in PN GSCs (L0627) by 2 different clones (sh*ASCL1_1* and sh*ASCL1_2*) followed by overexpression of *ASCL1* (*ASCL1* OE) results in the upregulation and downregulation of FUT8 protein accumulation and core fucosylation, respectively. Controls are defined as shEmpty Vector (shEV). Mean ± SEM over three biological replicates. Quantitative data are represented as bar graphs. Two-way ANOVA followed by a Tukey multiple comparison test. **B,** *ASCL1* overexpression in MES GSCs (L0315 and L1312) significantly reduces FUT8 protein accumulation, as observed in PN GSCs. FUT8 expression, normalized over calnexin, in mock versus ASCL1: L0315, **, $P < 0.01$; L1312; *, $P < 0.05$. Student t test, unpaired. **C,** FUT8 protein level decreases in early passage PN GSC cultures deriving from a MES GBM after they started expressing the PN classifier ASCL1. **D,** Xenografts induced by the intracranial transplantation of sh*ASCL1* PN GSCs show histological PMT features (H&E), which correlate with increased FUT8 level (FUT8, brown staining), when compared with sh*EV* controls. Quantification of FUT8 expression in the same xenografts ($n = 4$ different xenografts for each condition). ****, $P < 0.0001$, Student t test, unpaired; scale bars, 50 μm; insets, 10 μm. Specific staining for AALs (cytoplasmic, brown) is found in the cytoplasm of tumor cells in *ASCL1*-silenced PN xenografts (white arrowheads; insets), whereas it is absent in tumor cells in control xenografts (white arrows; insets). Scale bars, 50 μm; insets, 10 μm. **E,** Genomic views show ChIP-seq peaks for ASCL1 binding in *FUT8, GMDS* and *FPTG* genes. The peaks were derived from ChIP-seq data of human GBM GSCs (MGG8; pink profile) and multiple lung cancer cell lines obtained from independent laboratories (H1184, H1755, H2107, HCC4018, H128, and H889; blue and green profiles). The red highlight indicates the site screened by ChIP-qPCR in PN GSCs (L0627). **F,** ChIP-qPCR analysis shows binding of ASCL1 to promoter-binding sites of *FUT8, GMDS,* and *FPTG* genes in PN GSCs (L0627) expressing *ASCL1* either endogenously (Naïve GSCs; white and black bars, plots on the left) or ectopically (*ASCL1* GSCs; gray and red bars, plots on the right). Enrichment is shown as mean the percentage of input bound ± SEM over three biological replicates. Student t test, unpaired. *, $P < 0.05$; **, $P < 0.01$; ***, $P < 0.005$; ****, $P < 0.001$.
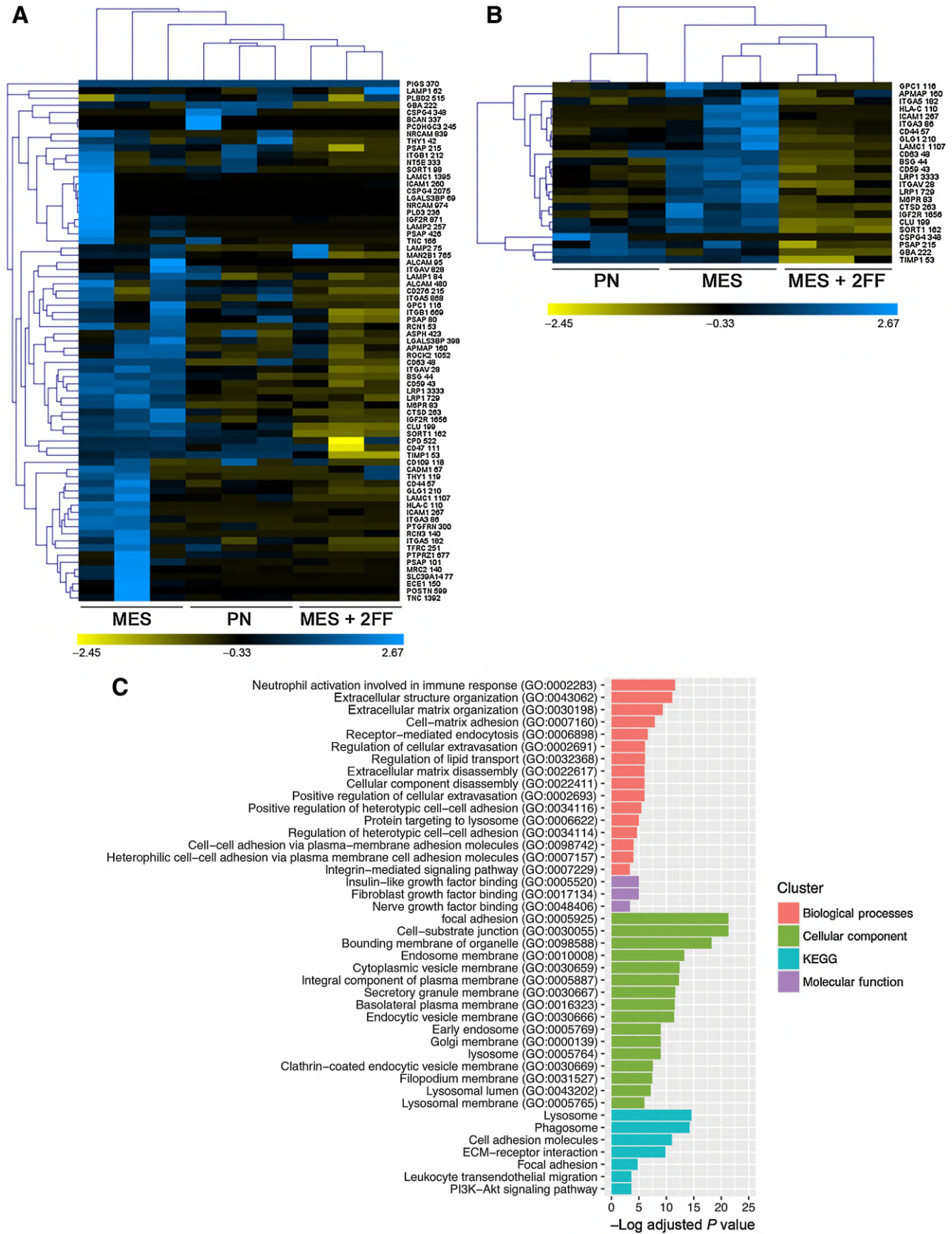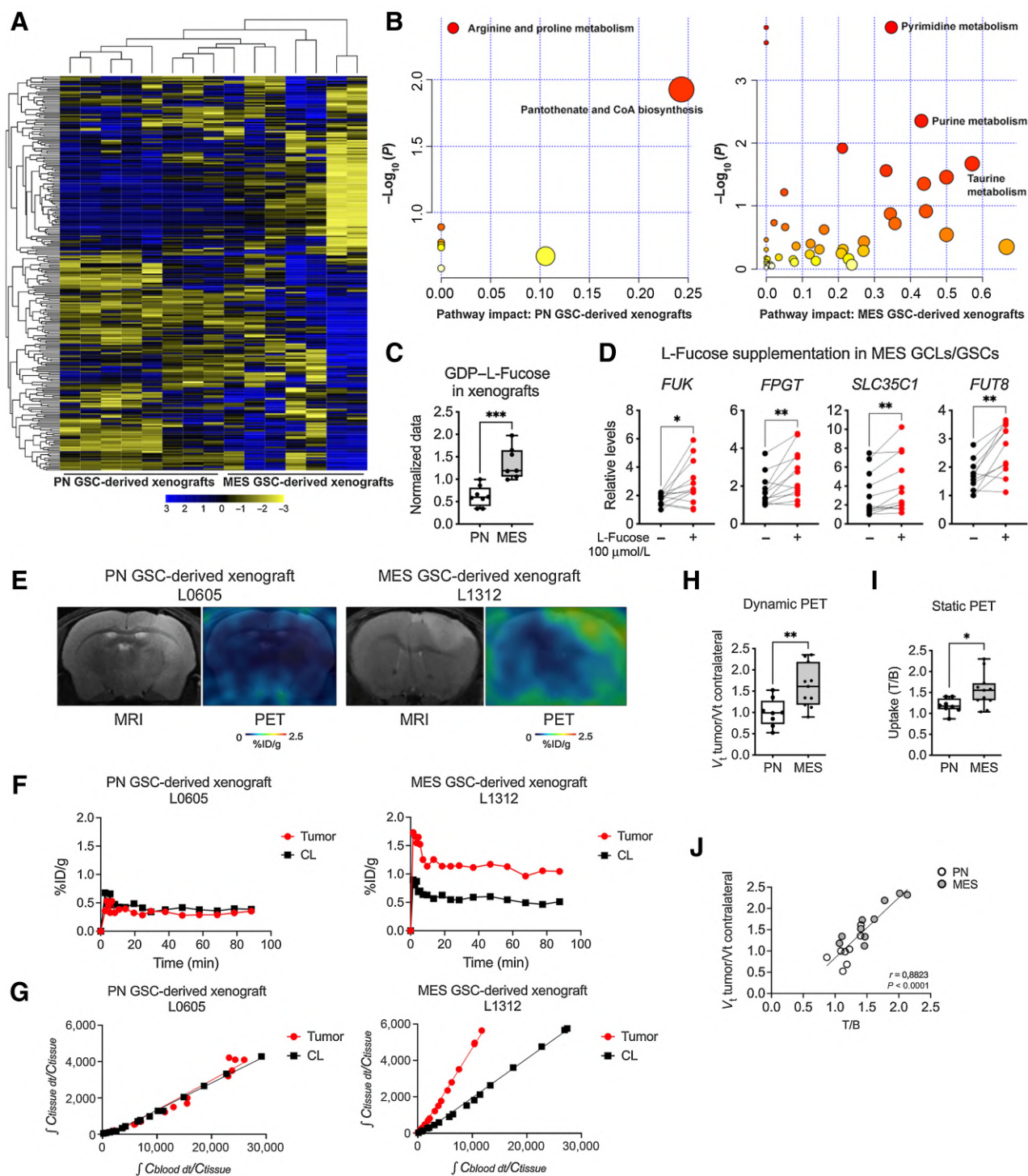
Figure 6.
Core-fucosylated glycoproteins are enriched in MES GSCs and are involved in biological processes relevant for the MES phenotype. (*Continued on the following page.*)

Figure 6.
(*Continued.*) **A,** Heat map clustering depicting the glycoprotein sites that are differentially core fucosylated in PN GSCs, MES GCLs/GSCs, and MES GCLs/GSCs treated with 2FF, as measured by LC/MS-MS–based glycoproteomics. Every single glycoprotein site is indicated by the corresponding gene name, followed by the number of the asparagine in the protein sequence. The yellow color indicates the lowest expression, whereas the blue the highest expression. **B,** Significantly different core-fucosylated sites in PN GSCs, MES GCLs/GSCs, and in MES GCLs/GSCs treated with 2FF are reported in the hierarchical clustering ($n = 24$; one-way ANOVA; $P < 0.1$). **C,** Gene Ontology (GO)- and KEGG-based annotation was used to perform functional enrichment analysis using the EnrichR tools. The adjusted $-\log P$ value represents the significance of the enrichment. The color key represents the four domains covered within the GO and the KEGG. Only annotations with a significant adjusted P value of <0.05 are shown. **D,** LC/MS-MS–based glycoproteomics show that ITGA3 and CD44 proteins are more highly core fucosylated in MES GCLs/GSCs than in PN GSCs and their core fucosylation is reduced by 2FF. The reported data refer to the peak intensity of each GlcNAcFuc peptide normalized to the intensity of the originating protein. Student t test, unpaired. **E,** ITGA3 and CD44 proteins are validated as being upregulated in MES GCLs/GSCs by WB. Densitometric quantification of ITGA3 and CD44 expression in the same samples. Student t test, unpaired. **F,** ITGA3 and CD44 proteins are retrieved only in MES GSC-derived xenografts; scale bars: 50 μm. **G,** LCA affinity enrichment of whole-cell lysates of MES GCLs/GSCs, treated or not with 2FF, followed by WB with ITGA3 and CD44 antibodies, indicates that the 2 proteins are core fucosylated, as their total level decreases upon 2FF treatment. Input shows no difference in the level of the total proteins. Densitometric quantification of ITGA3 and CD44 expressions in the same samples. One-way ANOVA followed by a Tukey multiple comparison test. **H,** LCA affinity enrichment of whole-cell lysates of *FUT8*-silenced MES GSCs, followed by WB with ITGA3 and CD44 antibodies, indicates that the 2 proteins are core fucosylated by FUT8, as their total level decreases upon *FUT8* knockdown. Input shows no difference in the level of the total proteins. Densitometric quantification of ITGA3 and CD44 expressions in the same samples. One-way ANOVA followed by a Tukey multiple comparison test. **I,** Time-lapse phase-contrast microscopy images of wound closure by sh*EV*, sh*FUT8_1* and sh*FUT8_2* MES GSCs (L1312) at 0 and 72 hours after wound generation. Quantification of the mean of the wounded areas filled by the migrating cells in each condition is expressed as relative wound density. Results represent the mean of 12 wells for each condition; $P < 0.0001$. *, $P < 0.05$; **, $P < 0.01$; ****, $P < 0.001$.

Figure 7.
Detection of L-Fucose accumulation in MES GCL/GSC-derived xenografts by preclinical PET. **A,** Hierarchical clustering of differentially represented metabolites identified and quantified by LC/MS-MS analysis in PN GSC- and MES GCL/GSC-derived xenografts (peak area). Yellow, lowest expression; blue, highest expression. **B,** Metabolic pathway analysis plots for PN GSC- and MES GCL/GSC-derived xenografts by MetaboAnalyst. The top pathways are ranked by the gamma-adjusted P values for permutation per pathway (y-axis) and the total number of hits per pathway (x-axis). The color grades from white to yellow, orange, and red as the values of both x and y axes increase. **C,** Normalized MS peak area of GDP-Fucose in PN GSC- and MES GCL/GSC-derived xenografts. Student t test, unpaired. **D,** All genes, coding for critical enzymes in the L-Fucose metabolic salvage pathway, are more highly expressed in MES GSC cultures after short-term medium supplementation with 100 μmol/L L-Fucose (RT-qPCR). Student t test, paired. The lines connect samples from each different MES GSC line (U87, U251, L1312, and L0315) before and after L-Fucose supplementation.   (*Continued on the following page.*)

same cells upon *in vivo* transplantation (49), few common metabolic pathways were conserved in subgroup-specific GSCs and in their corresponding xenografts (**Fig. 7B**; Supplementary Table S3). Among them, one common pathway enriched in both PN GSCs and in PN GSC-derived xenografts was the arginine and proline metabolism, whereas shared pathways between MES GCL/GSCs and their xenografts were the purine and the pyrimidine metabolism pathways (**Fig. 7B**; Supplementary Table S3). Most relevantly, like what detected in MES GSCs *in vitro*, GDP–L-Fucose, that is, the intermediate substrate that can be synthesized directly from L-Fucose, was significantly more abundant in MES than in PN xenografts (**Fig. 7C**), suggesting that the L-Fucose derivatives are accumulated in MES xenografts *in vivo*.

Next, to assess whether extracellular L-Fucose could be up taken in MES GBMs through the engagement of the salvage pathway, we supplemented the medium of PN GSCs and MES GCL/GSC lines with 100 μmol/L L-Fucose for 48 hours. Of note, the expression of the genes coding for the enzymes of the salvage pathway that are responsible for GDP–L-Fucose synthesis, transport, and glycan conjugation, that is, *FUK*, *FPGT*, *SLC35C1*, and *FUT8*, was significantly increased in all MES GSC lines after supplementation, whereas it was not affected in PN GSCs (**Fig. 7D**; Supplementary Fig. S13). Therefore, we hypothesized that a radiolabeled L-Fucose analogue could accumulate in MES tumor cells *in vivo* as well. In support of this hypothesis, the L-Fucose analogue 6-[18F]fluoro-L-Fucose (6-[18F]FF) was shown by autoradiography to accumulate in rat intracranial gliomas with a very high tumor-to-brain tissue ratio (50).

We tested the same radioactive tracer in NSG mice, intracranially transplanted with either PN GSCs or MES GCLs/GSCs ($n = 2$ PN GSC and $n = 3$ GCL/GSC lines, with 4 biological replicates for each cell line). When tumors were clearly detectable by MRI, mice were injected intravenously with 3.7 MBq of 6-[18F]FF and subjected to dynamic PET acquisitions lasting 90 minutes. 3D total body PET of healthy mice injected with 6-[18F]FF showed very low accumulation in non-targeted tissues, like the heart and the liver, and high accumulation in excretion organs, such as bladder and kidneys (Supplementary Fig. S14A). The kinetics of radioactivity distribution were calculated by manually drawing the VOIs in different body districts, including the tumor, the contralateral healthy brain parenchyma, heart, liver, and kidneys. Analysis of TACs showed that in both PN and MES xenografts the highest tracer accumulation was detected in the kidneys and the lowest in blood and liver (Supplementary Fig. S14B). Most remarkably, whereas tracer uptake in PN tumors was the same as in the contralateral hemisphere, the uptake in MES tumors was significantly higher and remained stable over time (**Fig. 7E–F**; Supplementary Table S4).

The distribution of a tracer in a tissue can be described in terms of compartments that can be either represented by a physical volume (*e.g.*, blood) or a chemical volume (*i.e.*, tracer bound to a receptor or enzyme). The time variation of the radioactivity in multicompartment systems can be calculated by either the Patlak or the Logan equations that define an irreversible trapping-compartment model or a reversible non–trapping-compartment model, respectively (refs. 51, 52; Supplementary Methods S1). To determine the best model that described the behavior of the 6-[18F]FF tracer in target (PN and MES xenografts) and non-target (contralateral parenchyma) tissues, we plotted $\int_0^T Ct\ dt$ (where C_t is the tissue VOI) divided by C_t at time $_T$ versus $\int_0^T Cb\ dt$ (where Cb is the heart cavity VOI) divided by C_t at time $_T$. Whereas the Patlak-based plots did not result in a good fitting of the data, the Logan-based plots were linear, thus demonstrating a reversible tracer exchange between tissue (either the contralateral hemisphere or the tumor) and blood during the time of acquisition in both types of xenografts (**Fig. 7G**). The R^2 values for the fits of the model were higher than 0.9 for all groups reflecting good quality linear fits (Supplementary Table S4). Notably, the ratio between the tissue distribution volume (V_t) of the tumor and the V_t of the contralateral hemisphere, which were calculated from the slope of the Logan plot curves (**Fig. 7G**), was significantly higher in MES xenograft-bearing mice than in the PN ones (regression analysis; $P < 0.0001$; **Fig. 7G** and **H**; Supplementary Table S4), indicating increased influx of 6-[18F]FF in the tumor cells of MES GCL/GSC-derived xenografts.

Mice were also subjected to static PET acquisitions, that is, 3 consecutive acquisitions of 30 minutes each (total length of acquisition: 90 minutes). Analysis of static PET acquisitions sampled between 60 and 90 minutes showed that the uptake of 6-[18F]FF expressed as tumor/background (T/B) ratios ranged from 1.52 up to 1.58 for MES xenografts and from 1.16 to 1.20 for PN xenografts, being significantly higher in MES xenografts (**Fig. 7I**). Of note, dynamic V_t and static T/B ratio values were significantly correlated, implying that static acquisition protocols may be sufficiently informative for 6-[18F]FF uptake data extrapolation (**Fig. 7J**).

Overall, our results indicate that the dynamics of 6-[18F]FF build-up in MES GBMs reflected a reversible increased influx in tumor cells and, most relevantly, that 6-[18F]FF accumulates specifically in MES xenografts, implying its potential use as minimally invasive imaging biomarker for MES GBM.

Discussion

Cancer metabolism implies the existence of convergent and divergent metabolic phenotypes that are differently actionable. Therapies against convergent core metabolic phenotypes that are shared by different cancers may have a broad utility, but, because these pathways are often active also in nonmalignant cells, their druggability is limited by a low therapeutic index. Conversely, divergent metabolic features that are restricted to tumor subtypes may result in acceptable toxicity profiles, with the advantage of developing patient-tailored therapeutic strategies (1).

(*Continued.*) **E,** Imaging of 6-[18F]FF uptake in PN GSC- and MES GSC-derived xenografts. Axial T2-weighted MRI images were co-registered with axial PET images. Radioactivity concentration values are expressed as the percentage of the injected dose per gram of tissue (%ID/g). **F,** Time activity curves of 6-[18F]FF uptake in the tumor and in the contralateral brain parenchyma of mice bearing PN GSC- and MES GSC-derived xenografts. Radioactivity concentration values are expressed as the percentage of the injected dose per gram of tissue (%ID/g). **G,** Graphical analysis of time–activity data from mice transplanted with PN GSCs and MES GCL/GSCs by the Logan equation. C refers to radioactivity in the volume of interest (VOI of tissue or blood) at time *t*. Regression analysis; $P < 0.0001$. **H,** The ratio between the tracer tissue distribution volume (V_t) in the tumor and the V_t in the contralateral parenchyma is significantly higher in MES GCL/GSC-derived xenografts than in PN. Student *t* test, unpaired. **I,** The uptake of 6-[18F]FF expressed as tumor/background (T/B) ratios is significantly higher in MES GCL/GSC-derived xenografts than in PN. Student *t* test, unpaired. **J,** 6-[18F]FF uptake as defined by dynamic PET acquisitions shows a significant positive correlation with the uptake determined by static PET acquisition performed at 60–90 minutes. Pearson *r*: 0.8860; R^2: 0.7850; $P < 0.0001$. *, $P < 0.05$; **, $P < 0.01$; ***, $P < 0.005$.

By taking advantage of the integrated analysis of the transcriptome, metabolome, and glycoproteome of subgroup-specific GSCs, we pinpointed L-Fucose and its malignancy-associated downstream metabolic process known as core fucosylation as divergent metabolic alterations that are specific of MES GBMs and that can be exploited both as MES-restricted biomarkers and therapeutic actionable targets.

Dysregulated fucosylation is one of the most important oligosaccharide modifications involved in cancer and is often caused by the aberrant expression of FUTs (53). α1,6-fucosyltransferase, which is encoded by the *FUT8* gene, mediates core fucosylation of GlcNAc linked to asparagine in the core of N-glycans and is upregulated in many different cancers, thus being considered as a promising prognostic cancer biomarker (53).

Fucosylated carbohydrate moieties are involved in a wide range of physiological and pathological processes, including cell adhesion, matrix interaction, epithelial-to-MES transition, fertilization, extravasation, and malignancy. Core-fucosylated proteins *per se* might be considered potential diagnostic and prognostic biomarkers. High levels of core-fucosylated alpha-fetoprotein in the serum of patients with HCC indicate cancer progression (54). Similarly, core-fucosylated prostate-specific antigen and haptoglobin are diagnostic for prostate and pancreatic cancer (24, 54).

In this context, also the MES-restricted core-fucosylated proteins that we identified through our glycoproteomic screen may serve as new MES GBM biomarkers. Many core-fucosylated proteins retrieved in MES GSCs share similar functions and are involved in the same biological processes, for example, integrin-mediated signaling, tumor cell adhesion and invasion, and interaction with the tumor microenvironment. For instance, like other integrins that were previously identified as putative GSC markers (55, 56), ITGA3 expression has been retrieved in GSCs and has been shown to correlate with migration and invasion (57). Similarly, CD44, a cell membrane glycoprotein involved in cell motility, proliferation, and angiogenesis, is again overexpressed in GSCs (58). Because core fucosylation is essential for the proper functioning of many different cancer-relevant proteins, such as EGFR, VEGFR, TGFβ1, and α3β1 signaling pathways (24), our data may provide additional refinement to the exploitation of membrane proteins as potential markers for GSCs. In fact, we add a further layer of molecular complexity, that is, the fucosylation status, to biomarker selection in GBM, by pinpointing biomarkers that are not only surrogate but also functional readouts for GSCs and whose cancer-promoting functions can be harnessed therapeutically.

From a mechanistic standpoint, metabolic reprogramming in cancer cells can take place through the coordinated dysregulation of all the enzymes that are part of the same synthetic pathway, as opposed to what is observed in normal cells, in which activation or inhibition of a single rate-limiting step enzyme is detected (11). The concerted dysregulation of many enzymes in the same pathway suggests the existence of a common upstream transcriptional regulator, as shown for the enzymes of the mevalonate and *de novo* purine synthesis pathways, which are controlled by MYC in GBM stem cells (11, 13). Along this line, here we demonstrate that the three genes coding for critical enzymes involved in L-Fucose biosynthesis and in core fucosylation, namely *FPGT*, *GMDS*, and *FUT8*, are transcriptionally repressed by the PN transcription factor ASCL1, which modulates PMT by repressing genes associated with the MES phenotype (31, 44). The finding that ASCL1 negatively regulates the expression of the key enzymes of the L-Fucose biosynthetic pathway not only provides mechanistic insights into the differential activation of the L-Fucose pathway in PN versus

MES GBMs but also highlights a potential role for the activation of this pathway in the definition and stabilization of MES features in the context of the PMT during GBM progression.

Malignant cells can also exploit the aberrant build-up of normal metabolites to increase their fitness. To date, only three metabolites are classified as *bona fide* oncometabolites, that is, 2HG, succinate and fumarate (59), which are defined as intermediates of metabolism that abnormally accumulate in cancer cells as a consequence of mutations of genes encoding the corresponding metabolic enzymes (60). Recently, it has been reported that 2HG is sufficient to promote tumorigenesis without underpinning IDH1 mutations, implying that also non-genetic alterations may contribute to tumorigenesis by increasing the accumulation of selected metabolites (61). Accordingly, glycine, sarcosine, and lactate have been proposed as putative oncometabolites even in the absence of genetic alterations in the enzymes regulating their synthesis (62). In this view, also L-Fucose might potentially be classified as a non-traditional oncometabolite for MES GBMs, because it selectively accumulates in MES GSCs and in their corresponding xenografts, likely through the coordinated upregulation of key pathway enzymes mediated by the downregulation of their transcriptional repressor ASCL1. Furthermore, L-Fucose supplementation in MES GSC cultures promotes the expression of the enzymes of the salvage pathway, suggesting a direct role of the metabolite in fueling its own metabolic pathway and, concurrently, promoting downstream post-translational protumorigenic events as core fucosylation, thus satisfying some of the cardinal features of oncometabolites.

Most relevantly, the preferential activation of core fucosylation in MES GBMs could be harnessed therapeutically for developing cancer precision medicine approaches aimed at designing molecularly stratified clinical trials. Small-molecule inhibitors of fucosylation have been successful in a variety of tumors, when tested preclinically (40–42). However, only one first-in-human, first-in-class clinical trial has directly addressed the therapeutic exploitability of fucosylation inhibitors, resulting in preliminary antitumor activity in patients with metastatic squamous cell carcinoma of the head and neck and breast cancer, with a few showing stable disease and a 50% reduction in tumor burden (NCT02952989; ref. 63). Regrettably, treatment with 2FF was associated with systemic thromboembolic events that led to study termination.

Precision medicine approaches are currently under development also for GBM treatment. Unfortunately, their implementation in the clinics has been burdened by several limitations, including (i) the inherent intratumor cellular and molecular heterogeneity and plasticity of GBM, which portends the requirement for multi-targeted therapies, (ii) the scarce delivery of drugs to the tumor, which is critical for the efficacy of molecularly targeted drugs, and (iii) the lack of suitable biomarkers for patient selection and longitudinal monitoring of tumor progression (64).

In this regard, we believe that the results of our preclinical trials might deliver significant insights into these issues.

First, we report that global inhibition of core fucosylation in MES GBM xenografts significantly reduces their growth, thus implying that interfering at the same time with the function of many different target glycoproteins might prevent the development of therapy resistance, which is often observed with single-targeted drugs. In addition, it has been also reported that removal of core fucose residues plays a key role also in modulating the contribution of the tumor microenvironment. Indeed, inhibition of fucosylation increases antibody-dependent cell-mediated cytotoxicity (40, 42) and decreases the cell-surface expression of PD-1 on T cells (65),

overall promoting antitumor immune responses that might be critical in immunologically "cold" tumors as GBMs. Thus, impairing fucosylation in a wide-range and comprehensive fashion by targeting both tumor and non-tumor cells might give rise to an effective anti-GBM combination strategy. Given the lack of competing therapies for GBM, molecularly actionable targets, even if present only in a subpopulation of tumor cells, remain a very attractive tool when tailoring treatment for individual patients, provided that this population is functionally critical for tumor fitness and therapy resistance, as the MES GBM cell component is (64).

Second, our *in vivo* experimental set up suggests that intratumor delivery strategies that circumvent the limitations posed by the presence of the blood–brain barrier might elicit durable response in terms of disease control, while preventing the systemic toxicity associated with the use of small molecule fucosylation inhibitors.

Finally, the possibility to specifically detect the accumulation of L-Fucose in MES GBM *in vivo* by PET-based minimally invasive imaging might help to precisely classify patients that are not eligible to surgery. L-Fucose monitoring will make feasible to measure therapy-induced fluctuations in subgroup affiliation that might take place during tumor progression and that need to be taken into consideration when considering alternative/second-line therapeutic options.

Overall, our results indicate that L-Fucose pathway hyperactivation and core fucosylation act in concert to determine therapeutic vulnerabilities in MES GBMs that represent patient-restricted phenotypes able to predict responsiveness to a therapy.

Authors' Disclosures

No disclosures were reported.

Authors' Contributions

V. Pieri: Conceptualization, formal analysis, validation, investigation, visualization, methodology, writing–original draft, writing–review and editing. **A.L. Gallotti:** Formal analysis, investigation. **D. Drago:** Validation, investigation, methodology. **M. Cominelli:** Validation. **I. Pagano:** Formal analysis, validation. **V. Conti:** Investigation, methodology. **S. Valtorta:** Validation, methodology. **A. Coliva:** Methodology. **S. Lago:** Investigation, visualization. **D. Michelatti:** Investigation. **L. Massimino:** Data curation, software. **F. Ungaro:** Software. **L. Perani:** Methodology. **A. Spinelli:** Methodology. **A. Castellano:** Methodology. **A. Falini:** Resources. **A. Zippo:** Resources. **P.L. Poliani:** Validation. **R. Moresco:** Validation, methodology. **A. Andolfo:** Validation, investigation, methodology. **R. Galli:** Conceptualization, resources, data curation, supervision, funding acquisition, investigation, methodology, writing–original draft, project administration, writing–review and editing.

Note

Supplementary data for this article are available at Cancer Research Online (http://cancerres.aacrjournals.org/).

References

1. Kim J, DeBerardinis RJ. Mechanisms and implications of metabolic heterogeneity in cancer. Cell Metab 2019;30:434–46.
2. Timmerman LA, Holton T, Yuneva M, Louie RJ, Padro M, Daemen A, et al. Glutamine sensitivity analysis identifies the xCT antiporter as a common triple-negative breast tumor therapeutic target. Cancer Cell 2013;24:450–65.
3. Goodwin J, Neugent ML, Lee SY, Choe JH, Choi H, Jenkins DMR, et al. The distinct metabolic phenotype of lung squamous cell carcinoma defines selective vulnerability to glycolytic inhibition. Nat Commun 2017; 8:15503.
4. Louis DN, Perry A, Wesseling P, Brat DJ, Cree IA, Figarella-Branger D, et al. The 2021 WHO classification of tumors of the central nervous system: a summary. Neuro Oncol 2021;23:1231–51.
5. Phillips HS, Kharbanda S, Chen R, Forrest WF, Soriano RH, Wu TD, et al. Molecular subclasses of high-grade glioma predict prognosis, delineate a pattern of disease progression, and resemble stages in neurogenesis. Cancer Cell 2006;9: 157–73.
6. Wang Q, Hu B, Hu X, Kim H, Squatrito M, Scarpace L, et al. Tumor evolution of glioma-intrinsic gene expression subtypes associates with immunological changes in the microenvironment. Cancer Cell 2017;32:42–56.
7. Nicholson JG, Fine HA. Diffuse glioma heterogeneity and its therapeutic implications. Cancer Discov 2021;11:575–90.
8. Patel AP, Tirosh I, Trombetta JJ, Shalek AK, Gillespie SM, Wakimoto H, et al. Single-cell RNA-seq highlights intratumoral heterogeneity in primary glioblastoma. Science 2014;344:1396–401.
9. Neftel C, Laffy J, Filbin MG, Hara T, Shore ME, Rahme GJ, et al. An integrative model of cellular states, plasticity, and genetics for glioblastoma. Cell 2019;178: 835–49.
10. Bhat KP, Balasubramaniyan V, Vaillant B, Ezhilarasan R, Hummelink K, Hollingsworth F, et al. Mesenchymal differentiation mediated by NF-kappaB promotes radiation resistance in glioblastoma. Cancer Cell 2013; 24:331–46.
11. Wang X, Yang K, Xie Q, Wu Q, Mack SC, Shi Y, et al. Purine synthesis promotes maintenance of brain tumor-initiating cells in glioma. Nat Neurosci 2017;20: 661–73.
12. Wang X, Yang K, Wu Q, Kim LJY, Morton AR, Gimple RC, et al. Targeting pyrimidine synthesis accentuates molecular therapy response in glioblastoma stem cells. Sci Transl Med 2019;11:eaau4972.
13. Wang X, Huang Z, Wu Q, Prager BC, Mack SC, Yang K, et al. MYC-regulated mevalonate metabolism maintains brain tumor-initiating cells. Cancer Res 2017; 77:4947–60.
14. Silver DJ, Roversi GA, Bithi N, Wang SZ, Troike KM, Neumann CK, et al. Severe consequences of a high-lipid diet include hydrogen sulfide dysfunction and enhanced aggression in glioblastoma. J Clin Invest 2021;131:e138276.
15. Puca F, Yu F, Bartolacci C, Pettazzoni P, Carugo A, Huang-Hobbs E, et al. Medium-Chain Acyl-CoA dehydrogenase protects mitochondria from lipid peroxidation in glioblastoma. Cancer Discov 2021;11:2904–23.
16. Jung J, Kim LJ, Wang X, Wu Q, Sanvoranart T, Hubert CG, et al. Nicotinamide metabolism regulates glioblastoma stem cell maintenance. JCI Insight 2017;2: e90019.
17. Wang LB, Karpova A, Gritsenko MA, Kyle JE, Cao S, Li Y, et al. Proteogenomic and metabolomic characterization of human glioblastoma. Cancer Cell 2021;39: 509–28.
18. Garofano L, Migliozzi S, Oh YT, D'Angelo F, Najac RD, Ko A, et al. Pathway-based classification of glioblastoma uncovers a mitochondrial subtype with therapeutic vulnerabilities. Nat Cancer 2021;2:141–56.

19. Blanas A, Sahasrabudhe NM, Rodriguez E, van Kooyk Y, van Vliet SJ. Fuco-sylated antigens in cancer: an alliance toward tumor progression, metastasis, and resistance to chemotherapy. Front Oncol 2018;8:39.

20. Zhou Y, Fukuda T, Hang Q, Hou S, Isaji T, Kameyama A, et al. Inhibition of fucosylation by 2-fluorofucose suppresses human liver cancer HepG2 cell proliferation and migration as well as tumor formation. Sci Rep 2017; 7:11563.

21. Agrawal P, Fontanals-Cirera B, Sokolova E, Jacob S, Vaiana CA, Argibay D, et al. A systems biology approach identifies FUT8 as a driver of melanoma metastasis. Cancer Cell 2017;31:804–19.

22. Wang X, Chen J, Li QK, Peskoe SB, Zhang B, Choi C, et al. Overexpression of alpha (16), fucosyltransferase associated with aggressive prostate cancer. Glycobiology 2014;24:935–44.

23. Tu CF, Wu MY, Lin YC, Kannagi R, Yang RB. FUT8 promotes breast cancer cell invasiveness by remodeling TGF-beta receptor core fucosylation. Breast Cancer Res 2017;19:111.

24. Liao C, An J, Yi S, Tan Z, Wang H, Li H, et al. FUT8 and protein core fucosylation in tumours: from diagnosis to treatment. J Cancer 2021;12:4109–20.

25. Wei KC, Lin YC, Chen CH, Chu YH, Huang CY, Liao WC, et al. Fucosyl-transferase 8 modulates receptor tyrosine kinase activation and temozolomide resistance in glioblastoma cells. Am J Cancer Res 2021;11:5472–84.

26. Galli R, Binda E, Orfanelli U, Cipelletti B, Gritti A, De Vitis S, et al. Isolation and characterization of tumorigenic, stem-like neural precursors from human glioblastoma. Cancer Res 2004;64:7011–21.

27. Richards LM, Whitley OKN, MacLeod G, Cavalli FMG, Coutinho FJ, Jaramillo JE, et al. Gradient of developmental and injury response transcriptional states defines functional vulnerabilities underpinning glioblastoma heterogeneity. Nat Cancer 2021;2:157–73.

28. Bowman RL, Wang Q, Carro A, Verhaak RG, Squatrito M. GlioVis data portal for visualization and analysis of brain tumor expression datasets. Neuro Oncol 2017; 19:139–41.

29. Orzan F, Pagani F, Cominelli M, Triggiani L, Calza S, De Bacco F, et al. A simplified integrated molecular and immunohistochemistry-based algorithm allows high accuracy prediction of glioblastoma transcriptional subtypes. Lab Invest 2020;100:1330–44.

30. Reynolds BA, Rietze RL. Neural stem cells and neurospheres—re-evaluating the relationship. Nat Methods 2005;2:333–6.

31. Narayanan A, Gagliardi F, Gallotti AL, Mazzoleni S, Cominelli M, Fagnocchi L, et al. The proneural gene ASCL1 governs the transcriptional subgroup affiliation in glioblastoma stem cells by directly repressing the mesenchymal gene NDRG1. Cell Death Differ 2019;26:1813–31.

32. Zhou J, Yang W, Hu Y, Hoti N, Liu Y, Shah P, et al. Site-Specific fucosylation analysis identifying glycoproteins associated with aggressive prostate cancer cell lines using tandem affinity enrichments of intact glycopeptides followed by mass spectrometry. Anal Chem 2017;89:7623–30.

33. Mazzoleni S, Politi LS, Pala M, Cominelli M, Franzin A, Sergi SL, et al. Epidermal growth factor receptor expression identifies functionally and molecularly distinct tumor-initiating cells in human glioblastoma multiforme and is required for gliomagenesis. Cancer Res 2010;70:7500–13.

34. Allen M, Bjerke M, Edlund H, Nelander S, Westermark B. Origin of the U87MG glioma cell line: good news and bad news. Sci Transl Med 2016;8:354re3.

35. Pang Z, Chong J, Zhou G, de Lima Morais DA, Chang L, Barrette M, et al. MetaboAnalyst 5.0: narrowing the gap between raw spectra and functional insights. Nucleic Acids Res 2021;49:W388–W96.

36. Laks DR, Crisman TJ, Shih MY, Mottahedeh J, Gao F, Sperry J, et al. Large-scale assessment of the gliomasphere model system. Neuro Oncol 2016;18:1367–78.

37. Ceccarelli M, Barthel FP, Malta TM, Sabedot TS, Salama SR, Murray BA, et al. Molecular profiling reveals biologically discrete subsets and pathways of pro-gression in diffuse glioma. Cell 2016;164:550–63.

38. Cancer Genome Atlas Research N. Comprehensive genomic characterization defines human glioblastoma genes and core pathways. Nature 2008;455:1061–8.

39. Li J, Hsu HC, Mountz JD, Allen JG. Unmasking fucosylation: from cell adhesion to immune system regulation and diseases. Cell Chem Biol 2018;25:499–512.

40. Okeley NM, Alley SC, Anderson ME, Boursalian TE, Burke PJ, Emmerton KM, et al. Development of orally active inhibitors of protein and cellular fucosylation. Proc Natl Acad Sci U S A 2013;110:5404–9.

41. Kizuka Y, Nakano M, Yamaguchi Y, Nakajima K, Oka R, Sato K, et al. An alkynyl-fucose halts hepatoma cell migration and invasion by inhibiting GDP–fucose-synthesizing enzyme FX, TSTA3. Cell Chem Biol 2017;24:1467–78.

42. Disis ML, Corulli LR, Gad EA, Koehnlein MR, Cecil DL, Senter PD, et al. Therapeutic and prophylactic antitumor activity of an oral inhibitor of fucosyla-tion in spontaneous mammary cancers. Mol Cancer Ther 2020;19:1102–9.

43. Nwagwu CD, Immidisetti AV, Jiang MY, Adeagbo O, Adamson DC, Carbonell AM. Convection enhanced delivery in the setting of high-grade gliomas. Pharmaceutics 2021;13:561.

44. Park NI, Guilhamon P, Desai K, McAdam RF, Langille E, O'Connor M, et al. ASCL1 reorganizes chromatin to direct neuronal fate and suppress tumorige-nicity of glioblastoma stem cells. Cell Stem Cell 2017;21:209–24.

45. Stringer BW, Day BW, D'Souza RCJ, Jamieson PR, Ensbey KS, Bruce ZC, et al. A reference collection of patient-derived cell line and xenograft models of pro-neural, classical and mesenchymal glioblastoma. Sci Rep 2019;9:4902.

46. Rheinbay E, Suva ML, Gillespie SM, Wakimoto H, Patel AP, Shahid M, et al. An aberrant transcription factor network essential for Wnt signaling and stem cell maintenance in glioblastoma. Cell Rep 2013;3:1567–79.

47. Borromeo MD, Meredith DM, Castro DS, Chang JC, Tung KC, Guillemot F, et al. A transcription factor network specifying inhibitory versus excitatory neurons in the dorsal spinal cord. Development 2014;141:3102.

48. Augustyn A, Borromeo M, Wang T, Fujimoto J, Shao C, Dospoy PD, et al. ASCL1 is a lineage oncogene providing therapeutic targets for high-grade neuroendo-crine lung cancers. Proc Natl Acad Sci U S A 2014;111:14788–93.

49. Liao C, Glodowski CR, Fan C, Liu J, Mott KR, Kaushik A, et al. Integrated metabolic profiling and transcriptional analysis reveals therapeutic modal-ities for targeting rapidly proliferating breast cancers. Cancer Res 2022;82: 665–80.

50. Ishiwata K, Tomura M, Ido T, Iwata R, Sato K, Hatazawa J, et al. 6-[18F]fluoro-L-fucose: a possible tracer for assessing glycoconjugate synthesis in tumors with positron emission tomography. J Nucl Med 1990;31:1997–2003.

51. Patlak CS, Blasberg RG. Graphical evaluation of blood-to-brain transfer con-stants from multiple-time uptake data. Generalizations. J Cereb Blood Flow Metab 1985;5:584–90.

52. Logan J, Fowler JS, Volkow ND, Wolf AP, Dewey SL, Schlyer DJ, et al. Graphical analysis of reversible radioligand binding from time-activity measurements applied to [N-11C-methyl]-(-)-cocaine PET studies in human subjects. J Cereb Blood Flow Metab 1990;10:740–7.

53. Bastian K, Scott E, Elliott DJ, Munkley J. FUT8 Alpha-(16)-Fucosyltransferase, in Cancer. Int J Mol Sci 2021;22:455.

54. Schneider M, Al-Shareffi E, Haltiwanger RS. Biological functions of fucose in mammals. Glycobiology 2017;27:601–18.

55. Lathia JD, Gallagher J, Heddleston JM, Wang J, Eyler CE, Macswords J, et al. Integrin alpha 6 regulates glioblastoma stem cells. Cell Stem Cell 2010;6: 421–32.

56. Haas TL, Sciuto MR, Brunetto L, Valvo C, Signore M, Fiori ME, et al. Integrin alpha7 is a functional marker and potential therapeutic target in glioblastoma. Cell Stem Cell 2017;21:35–50.

57. Nakada M, Nambu E, Furuyama N, Yoshida Y, Takino T, Hayashi Y, et al. Integrin alpha3 is overexpressed in glioma stem-like cells and promotes invasion. Br J Cancer 2013;108:2516–24.

58. Mooney KL, Choy W, Sidhu S, Pelargos P, Bui TT, Voth B, et al. The role of CD44 in glioblastoma multiforme. J Clin Neurosci 2016;34:1–5.

59. Liu Y, Yang C. Oncometabolites in cancer: current understanding and chal-lenges. Cancer Res 2021;81:2820–3.

60. Collins RRJ, Patel K, Putnam WC, Kapur P, Rakheja D. Oncometabolites: a new paradigm for oncology, metabolism, and the clinical laboratory. Clin Chem 2017; 63:1812–20.

61. Sciacovelli M, Frezza C. Oncometabolites: unconventional triggers of oncogenic signalling cascades. Free Radic Biol Med 2016;100:175–81.

62. Beyoglu D, Idle JR. Metabolic rewiring and the characterization of oncometa-bolites. Cancers 2013;13:2900.

63. Do KT, Chow LQM, Reckamp K, Sanborn RE, Burris H, Robert F, et al. First-in-human, first-in-class, phase I trial of the fucosylation inhibitor SGN-2FF in patients with advanced solid tumors. Oncologist 2021;26: 925–e1918.

64. Ghiaseddin A, Hoang Minh LB, Janiszewska M, Shin D, Wick W, Mitchell DA, et al. Adult precision medicine: learning from the past to enhance the future. Neurooncol Adv 2021;3:vdaa145.

65. Okada M, Chikuma S, Kondo T, Hibino S, Machiyama H, Yokosuka T, et al. Blockage of core fucosylation reduces cell-surface expression of PD-1 and promotes antitumor immune responses of T cells. Cell Rep 2017;20:1017–28.